Revision 2

Hyper-enrichment of heavy rare earth element in highly evolved granites through multiple hydrothermal mobilization

Martin Yan Hei Li, Mei-Fu Zhou

Institute of Geochemistry, Chinese Academy of Sciences, Guiyang 550081, China

---

Corresponding author: Martin Yan Hei Li

Email: martinyhli@gmail.com

Corresponding author: Mei-Fu Zhou

Email: zhoumeifu@hotmail.com

Abstract

Highly evolved granites can be important hosts of rare earth element (REE) resources, and more importantly, they commonly serve as the protolith for regolith-hosted REE deposits to form during weathering. Highly evolved granites in the Zudong pluton, South China are extremely rich in the HREE (up to 8,000 ppm total HREE) and display significant REE fractionation. Moreover, the HREE enrichment is positively correlated with the degree of REE fractionation, indicating a unique process in preferentially enriching the HREE during the evolution of the granites. Multiple stages of hydrothermal re-mobilization of the REE can account for the HREE mineralization and these are recorded in the texture and composition of the zircon. In these processes, fluctuations in the F activity of the fluid caused alternating dissolution-reprecipitation and continuous growth of the zircon. REE were repeatedly mobilized and enriched in the fluid to precipitate the major HREE mineral synchysite-(Y), and partially incorporated into the growth zone of zircon while other elements were largely lost to the fluid during extensive dissolution of the rock-forming minerals. LREE were also likely substantially mobilized in the late hydrothermal stage and lost through complexation with Cl, causing the significant LREE depletion and thus REE fractionation. This process continuously enriched host granites in the HREE to a potentially economic grade, making them favorable protoliths for subsequent supergene regolith-hosted HREE deposits.

Key words: Rare earth element (REE), HREE mineralization, zircon, hydrothermal alteration, highly evolved granite

1. Introduction

Rare earth element (REE) include lanthanide elements and yttrium (Y). These elements show similar geochemical behavior but can be fractionated strongly in various geological environments (Henderson, 2013). Thus, they can be used to trace a variety of natural processes, including the evolution of melts and fluids in magmatic-hydrothermal systems (e.g., Bea, 1996; Hanchar and Van Westrenen, 2007; Migdisov et al., 2016; Williams-Jones et al., 2012). Recently, these elements have become increasingly important in various high-technological applications for a carbon-neutral society, especially for the heavy (H)REE. Magmatic-hydrothermal systems may form REE deposits associated with granites, carbonatites and other alkaline complexes (Verplanck et al., 2016; Williams-Jones et al., 2012). Whereas, most of these REE-rich rocks are light (L)REE-dominated, HREE-dominated rocks have been rarely discovered, essentially restricted to highly evolved granites (Li et al., 2019; Li et al., 2017; Sanematsu and Watanabe, 2016). The HREE-rich rocks are important HREE resources, and more importantly, through weathering, they form the regolith-hosted REE deposits (Li et al., 2017) that supply more than 85% of the global HREE production (U.S. Geological Survey, 2023).

Generally, the HREE can be concentrated in highly evolved granitic melts by removal of major elements and LREE through fractional crystallization (Bea et al., 1994; Breiter et al., 1997). Volatile-rich phases in these systems could be substantially rich in the REE (Bau, 1996; Irber, 1999; Vasyukova and Williams-Jones, 2018; Williams-Jones et al., 2000) and subsequent hydrothermal overprinting can enrich the granites with the HREE. Alternatively, upgrading of the HREE concentration can be achieved through metasomatism by externally-derived HREE-rich fluids (Fan et al., 2023; Xu et al., 2017). Hydrothermal alteration is generally agreed as the key process for the significant HREE enrichment in these highly evolved granites to a potentially economic grade (Li et al., 2017; Sanematsu and Watanabe,

2016). However, these processes causing the HREE enrichment have not been comprehensively illustrated, nor those responsible for the significant REE fractionation. Deciphering the mechanism involved in the HREE enrichment and REE fractionation would be important in understanding the magmatic-hydrothermal evolution of highly evolved systems. The knowledge also sheds light to HREE mineralization and ore formation.

The Zudong pluton in South China shows a sub ore-grade HREE concentration and significant REE fractionation, both of which are at the highest and the most extreme among all granites recorded in the GEOROC database [Fig. S1; Sarbas (2008)]. This pluton is also the protolith of the world's largest known regolith-hosted HREE deposit (Li et al., 2019). Thus, the Zudong pluton provides a valuable opportunity to investigate the HREE enrichment process in granitic system. Early study has causatively attributed hydrothermal alteration to the HREE enrichment (Huang et al., 1989), and a more recent study has compared the isotopic composition of different units of different degree of fractionation to trace the source of the hydrothermal fluid (Fan et al., 2023). However, how the HREE concentration was being upgraded during the hydrothermal alteration has not yet been well illustrated. In felsic igneous systems, zircon is a common REE-bearing accessory mineral and commonly records their magmatic-hydrothermal history (Chen and Zhou, 2017; Geisler et al., 2007; Schneider et al., 2012). Both melt and fluid dynamics can be archived by the chemical and structural changes of zircon (Geisler et al., 2007), and under certain circumstances, REE concentrations of the coeval melts or fluids can be inferred from the zircon chemistry (Hanchar and Van Westrenen, 2007). Thus, zircon can be used as a powerful tool to help reconstruct the magmatic-hydrothermal evolution of such systems. Although trace elemental compositions, combined with the crystallinity and texture, are commonly used to discriminate magmatic, metamict, and hydrothermal zircon (Wang et al., 2023; Yang et al., 2014; Zeng et al., 2017; Zhao et al., 2016), detailed characterization of consecutive growth zones that record the

magmatic to hydrothermal processes is rare but could potentially provide more in-depth illustration of the geochemical evolution of the system.

In this study, we document the highly evolved granites of the Zudong pluton in South China from mineral records. Through detailed characterization of the REE mineralization and the corresponding mineralogical and geochemical record preserved in the zircon grains, we elucidate the hydrothermal process for HREE enrichment and REE fractionation, and potential ore formation in these systems.

2. Geological background

The Zudong granitic pluton is located in the Nanling region of SE China. In this region, multiple tectono-thermal events have taken place episodically from Ordovician-Silurian to late Cretaceous generating voluminous highly evolved metaluminous to slightly peraluminous calc-alkaline I-type granites and A-type granites (Zhou et al., 2006), including the Zudong granite which formed at 168.2 ± 1.2 Ma according to a zircon U-Pb dating (Zhao et al., 2014). The Zudong pluton crops out over an area of 32.5 km^2 and intrudes early Jurassic volcanic rocks and late Permian coal-bearing shale and mudstone (Fig. 1). The pluton is composed of the lower unit of granodiorite and biotite granite and upper unit of muscovite-bearing alkali-feldspar granite [Fig. 1; Fan et al. (2023)]. Derived from weathering of the Zudong pluton, especially the muscovite-bearing alkali-feldspar granite, is the world's largest regolith-hosted HREE deposit, the Zudong deposit. The deposit hosts a pre-mining resource of 131,000 t of REE oxide at a grade of 0.05 wt. % RE oxide in weathering crust from a few to up to 30 m thick (Li et al., 2019; Li et al., 2017).

In the ore-forming muscovite-bearing granites, the major minerals include quartz, K-feldspar, albite, and muscovite (Fig. 2a). Accessory minerals that host most of the REE include zircon, xenotime-(Y), Y-bearing fluorite, synchysite-(Y), gadolinite-(Y), hingganite-

(Y), yttrialite-(Y), euxenite-(Y), and fergusonite-(Y). Persuasive overprinting is observed with albite largely replaced by muscovite ± quartz (Figs. 2b) and biotite by muscovite + hematite (Figs. 2c). Hematite also occurs along the cleavage planes of albite (Fig. 2d). Muscovite grains show no overprinting and are presumed to represent the last stage of alteration. Most REE minerals are disseminated in the granites and regarded as hydrothermal phases showing various crosscutting and replacement relationship to the major minerals and the primary REE minerals (Li et al., 2019). The HREE mineralization has been attributed to late-stage autometasomatism during the magmatic-hydrothermal transition of the granitic magma (Huang et al., 1989) or hydrothermal overprinting by externally derived HREE-rich fluid probably originated from the subducting slab (Fan et al., 2023).

3. Samples and analytical methods

In this study, 22 samples were collected across the muscovite-bearing granite unit that hosts the sub-ore grade HREE enrichment for petrographic and mineralogical analyses. The sampling locations are marked in Figure 1.

3.1 Morphology and structure

Petrographic analysis was carried out with optical, electronic, and cathodoluminescence microscopy. The scanning electron microscope (SEM) used are equipped with an Oxford INCAx-sight energy-dispersive spectroscopic (EDS) detector operating at 20 kV and 60 - 80 μA for preliminary mineral identification. Raman spectroscopy on zircon grains was undertaken with the RISE microscopy system at the State Key Laboratory of Biogeology and Environmental Geology, China University of Geosciences, Wuhan (CUGW). This system enables simultaneous Raman and SEM analysis,

comprising an Alpha 300-R Laser Raman spectrometer and a Tescan VEGA 3 SEM. The adapted laser wavelength is 532 nm with the power of 6 mW and integration time of 5 s.

3.2 Whole-rock major and trace elements

Major element concentrations were determined using fused glass beads after the loss of ignition determination on an AxiomAX-Advanced X-ray fluorescence spectrometer in the University of Hong Kong. The analytical accuracy and precision are of <0.5%. Trace element concentrations were measured with an Agilent 7900 inductively coupled plasma mass spectrometer (ICP-MS) after mixed acid digestion of the fused glass beads. Both the accuracy and precision were <10% for all elements analyzed. Fluorine concentrations were determined potentiometrically by a specific ion electrode after potassium hydroxide fusion. The detection limit is 20 ppm. Carbon concentration hosted as carbonate minerals is measured by ethanolamine coulometer as CO_2 after digestion with $HClO_4$. The detection limit is 0.2%.

3.3 Chemical composition of zircon

3.3.1 Major and minor elements

Compositions of zircon grains were analyzed with a JEOL JXA-8230 electron microprobe in the University of Hong Kong, under a 20 kV accelerating voltage, a 20 nA beam current, and a 1 μm beam spot diameter. The analyzing crystals were PET (Zr, Hf, Ca, U, Th, P, Y, and Cl), LiF (Gd, Dy, Er, Yb, Fe, and Ti), LED1 (F), and TAP (Si and Al). Counting times on the peak positions were 40 s for REE, Hf, Th, and U; 20 s for Zr, P, Si, Al, Ca, Fe, and Ti and 10 s for F, and Cl. Representative background intensities were measured on both sides of the peak for half of the peak time. The Kα line was chosen for the analyses of P, Si, Al, Ca, Fe, Ti, F, and Cl; the Lα for Zr, Hf, and Y; the Lβ line for Gd, Dy, Er, and Yb; and the Mα line for Th and U. The standards are zircon for Zr, orthoclase for Si and Al,

apatite for Ca and P, magnetite for Fe, rutile for Ti, YP_5O_{14} for Y, monazite for Gd and Th, DyP_5O_{14} for Dy, ErP_5O_{14} for Er, YbP_5O_{14} for Yb, Hf metal for Hf, coffinite for U, topaz for F, and tugtupite for Cl. Detection limits were generally ~100 - 200 ppm. All data were corrected using standard ZAF correction procedures. Elemental mapping was carried out on selected zircon grains under a 20 kV accelerating voltage, a 20 nA beam current, a 1 μm beam spot diameter and a dwell time of 500 μs. Mapping was achieved through rastering the designated area with continuous spots.

3.3.2 Trace elements

Trace elemental analyses of zircon grains were conducted using a GeoLas 2005 laser ablation system with an Agilent 7900 ICP-MS at the State Key Laboratory of Geological Processes and Mineral Resources, CUGW. Laser pulses of 16 - 24 μm diameter at 5 Hz ablated the surfaces of the sample for about 50 s after monitoring the gas blank for approximately 20 s. All analytical spots were checked under optical microscope and SEM before analysis to avoid ablating the mineral inclusions. The generated aerosols were carried by a helium carrier gas and mixed with argon make-up gas via a T-connector before entering the ICP-MS instrument for acquisition of ion-signal intensities. Rare earth element compositions of zircon were externally calibrated against various reference materials (NIST SRM 610, BHVO-2G, BCR-2G, and BIR-1G) without using an internal standard. Data reduction was carried out with the ICPMSDataCal program.

4. Results

4.1 Occurrence of REE-bearing minerals

Complementary to the observations by Li et al. (2019), further petrographic examination reveals the paragenesis of various REE-bearing phases of the Zudong granite.

The main REE minerals are REE fluorocarbonate [notably synchysite-(Y)], REE-bearing fluorite, and the REE silicates, mainly gadolinite-(Y), hingganite-(Y), and yttrialite-(Y), and a minor amount of zircon and thorite. Minor amount of REE phosphates, mainly xenotime-(Y), and REE niobates, including fergusonite-(Y) and euxenite-(Y) are also observed.

REE silicates: Gadolinite-(Y) and yttrialite-(Y) often co-exist and occur in voids in albite (Fig. 3a). Both minerals are often in granular form but gadolinite-(Y) can also be in irregular patchy shape (Fan et al., 2023), whereas hingganite-(Y) occurs in radiating prismatic form and as mesh-textured veinlets along albite cleavage plane (Fig. 3b). The hingganite-(Y) veinlets often include rounded, anhedral calcite in the core (Fig. 3c). Occurrence of zircon will be described in the following section. The REE silicates are locally cut by fluorite and synchysite-(Y) (Figs. 3d & e).

Fluorite: Fluorite is commonly interstitial to the major minerals, or, less commonly, fills veinlets and small pods where it mainly replaces albite (Fig. 3f). In some places, fluorite veinlets cut hingganite-(Y) veinlets (Fig. 3e). Two varieties of fluorite are observable under the BSE imaging. One is clean, REE-enriched and BSE-bright (Flr-1), while the other one is porous, relatively REE-depleted, and BSE-dark (Flr-2). The Flr-2 is associated with inclusions of synchysite, and cut and embayed the Flr-1 (Fig. 3g).

Synchysite: From EDS analysis, both synchysite-(Y), enriched in Y and the HREE, and synchysite-(Ce), enriched in the LREE, are identified (See the Supplementary Information for representative EDS spectra and analytical results). Synchysite-(Y) appears as either subhedral to euhedral laths replacing calcite, irregular-pods interstitial to feldspar and muscovite, or inclusions in fluorite. In fluorite and synchysite-(Y), inclusions of synchysite-(Ce) in variably irregular shape and variable size are common. The synchysite-(Ce) inclusions are also often corroded and embayed (Figs. 3h – j). From the BSE imaging and EDS analysis, two compositional varieties of synchysite-(Y) can be observed, one less

enriched in the HREE, except Y (referred thereinafter Syn-1), and the other more enriched in the HREE (Syn-2). Syn-2 occurs as diffuse bands cutting Syn-1, whereas Syn-1 often shows a porous core and a narrow, clean rim in an individual grain (Fig. 3j).

Xenotime, fergusonite-(Y), euxenite-(Y), and thorite. Xenotime and REE niobates are often rounded and corroded (Figs. 3k & l) and occur mainly as inclusions in mica. In some samples, anhedral xenotime and euxenite-(Y) grains are spatially associated with synchysite-(Y) and occur together as vein-filling phases. Thorite is also highly corroded and embayed, particularly when associated with fluorite and the fluorocarbonates.

4.2 Petrography of zircon

Individual zircon grains from the Zudong granites are variable in size from 20 to 150 μm long and in shape from anhedral and rounded to subhedral and tabular shape with pyramidal tips. Complicated textures are also shown that generally include up to 5 distinct domains (Fig. 4). Domain 1 has bright cathodoluminescence (CL) but dim BSE images, rounded cores, and oscillatory zoning. Domain 2, which commonly rims Domain 1, is porous, with dark CL but bright BSE images, and contains abundant inclusions of xenotime and thorite. Domain 3 is a narrow, inclusion-free, growth zone, with dark CL and bright BSE images. It typically rims Domain 2 and, in turn, is typically rimmed by a wide overgrowth with dark CL and dim BSE images (Domain 4). In some cases, Domain 3 may be partially truncated or rimmed by another porous domain (collectively defined as Domain 2 referring to the porous texture), before rimmed by the Domain 4. Domain 4 is partially overprinted by irregular patches with dark CL and even dimmer BSE images that represent Domain 5. Raman analyses reveal that Domain 1 is crystalline with strong and sharp peaks at 1,004 – 1,010 cm^{-1}, 439 – 442 cm^{-1}, and 355 – 358 cm^{-1}, for the vibration bands of Si-O antisymmetric stretching, symmetric bending, and symmetric rotating, respectively. Weak

and broad bands at 995 – 1,001 cm^{-1}, probably represent the vibration band of Si-O antisymmetric stretching, are only observed in Domain 2; the other domains do not show any characteristic peaks of crystalline zircon in their spectra (Fig. 5).

In the granites, zircon is often included in fluorite and synchysite-(Y) (Fig. 6). In some samples, zircon grains are highly altered and largely dissolved, with the crystal shape and internal structure largely destroyed (Fig. 4). Zircon grains with Domain 2 in the core and Domain 4 overgrowth are included in, but overall in sharp and well-defined contact with, synchysite-(Y) (Fig. 6a & b). Also, growth zone of zircon (Domain 4) also occasionally cut synchysite-(Ce) (Fig. 6c), whereas being corroded by synchysite-(Y) (Fig. 6d).

4.3 Elemental composition of zircon

In total, 240 EPMA and 60 LA-ICPMS analyses of zircon compositions have been conducted. The entire dataset for zircon compositions is provided in Table S1 and S2, and presented in Fig. 7. Domain 1 has the highest and most clustered Zr concentrations of 63.96 ± 1.78 wt.% ZrO_2. Concentrations progressively decrease and become more dispersed in Domains 2 (57.02 ± 5.11 wt.%), 3 (50.45 ± 7.53 wt.%), and 5 (50.05 ± 6.03 wt.%). Zirconium concentrations in Domain 4 are comparatively high and constant (57.94 ± 2.45 wt.%) (Fig. 7). The concentrations of the non-formula elements, notably Al, P, REE, U, and Th, exhibit an opposite trend as Zr and increase from Domain 1 to the other domains, with the maxima in Domains 3 and 5 (Figs. 7 – 9; S2 – S4). For example, Y_2O_3 content increases from 0.35 wt.% in Domain 1 to 2.66 wt.%, 6.00 wt.%, 1.25 wt.%, 5.36 wt.% in Domain 2 to 5, respectively. Yb_2O_3 contents can reach up to 10 wt.%, and average Al_2O_3 contents of ~0.5 wt.% and P_2O_5 of 0.8 wt.%, respectively. Analytical results from LA-ICPMS analyses show similar trends (Fig. 10a). Exceptionally, Domain 4 has the highest Hf concentration, 4.72 wt.% HfO_2 on average, although Domains 2 (2.69 wt.%), 3 (2.71 wt.%), and 5 (4.14 wt.%) have

elevated concentrations (Figs. 7 - 10, Table S1; see also the supplementary dataset). From Domains 1 to 5, the zircons progressively become LREE-enriched, except Domain 4 which is relatively less LREE-enriched than Domain 3 and 5 [Average $(La/Yb)_N$ value of Domain 1: 0.0002; Domain 2: 0.0024; Domain 3: 0.0036; Domain 4: 0.0015; domain 5: 0.0028]. The zircons are also characterized by less positive Ce anomalies (Calculated as $Ce/Ce^* = Ce_N/(\sqrt{La_N \times Nd_N})$; Domain 1: 49.6; Domain 2: 1.96; Domain 3: 2.01; Domain 4: 2.15; Domain 5: 0.98) and more negative Eu (Calculated as $Eu/Eu^* = Eu_N/(\sqrt{Sm_N \times Gd_N})$; Domain 1: 0.099; Domain 2: 0.0065; Domain 3: 0.0056; Domain 4: 0.014; Domain 5: 0.0081) and Y anomalies (Calculated as $Y/Y^* = Y_N/(\sqrt{Ho_N \times Er_N})$; Domain 1: 0.78; Domain 2: 0.65; Domain 3: 0.65; Domain 4: 0.67; Domain 5: 0.59) (Fig. 10a; Table S2). The Ce and Eu anomalies are also calculated using least-square polynomial fitting developed in Anenburg and Williams (2022), the results (Table S2) are consistent with those presented above calculated by a linear interpolation.

4.4 Whole-rock geochemistry

Granites from the Zudong pluton is siliceous (SiO_2 content of 73 – 78 wt. %), aluminous (Al_2O_3 content of 12.1 – 14.4 wt. %), alkaline (Na_2O + K_2O content of 6 – 9 wt. %), and rich in F (2,420 – 3,870 ppm) and CO_2 (up to 0.6 wt. %). Geochemically, the granites have affinity from slightly peralkaline to peraluminous and belong to A-type granite based on the discriminant diagram of Eby (1990) (Fig. S5). They have variable total REE concentrations varying from ~150 to 7,700 ppm, of which ~80 – 95% are HREE (Fig. 10b; Table S3), but all the rocks are enriched in HREE [$(La/Yb)_N$ ratio of 0.1 - 0.6] (Fig. 10b). In addition, the proportions of HREE are higher [lower $(La/Yb)_N$ ratio] in granites of higher total REE concentrations. All analyzed samples have negative Eu anomalies (≤0.02) and variable Ce and Y anomalies (0.18 – 1.55 and 0.89 – 1.45, respectively). Interestingly, the

bulk REE concentrations of the granites of this study show a moderately to strongly positive correlation with bulk Al_2O_3 (r^2 = 0.69), F (r^2 = 0.64), Rb (r^2 = 0.78) concentrations, and LOI (r^2 = 0.83) value (Fig. 11), but a negative correlation with the magnitude of Ce anomalies (r^2 = 0.65) and $(La/Yb)_N$ ratios (r^2 = 0.83); the sample with the highest REE concentration (7,684 ppm) has the most negative Ce anomaly (0.18) and the lowest $(La/Yb)_N$ value (0.12). Furthermore, the $(La/Yb)_N$ values show a moderately negative correlation with Al_2O_3 (r^2 = 0.53) and Rb (r^2 = 0.47) concentrations (Fig. S6). The entire dataset for whole rock geochemical compositions is provided in Table S3. Tetrad effect exhibited on the chondrite-normalized pattern is further evaluated with the lambda shape coefficient after Anenburg and Williams (2022). The obtained tetrad coefficients (τ) are given in Table S3 and are generally positive, defining a M-type tetrad pattern. The Eu and Ce anomalies determined by this method (≤0.02 and 0.20 – 1.65, respectively) are comparable to the values presented above calculated by a linear interpolation.

5. Discussion

5.1 Origin and paragenesis of REE minerals

The major REE hosts in the Zudong granite, notably gadolinite-(Y), hingganite-(Y), yttrialite-(Y), synchysite-(Y), and fluorite, showed extensive replacement and veining texture against primary rock-forming minerals, suggesting a hydrothermal origin. Xenotime and REE niobates likely show two generations. The first one occurred as extensively altered, rounded, and corroded inclusions in mica. These grains were likely of a magmatic origin and represented the relict minerals survived after hydrothermal alteration. The other generation is represented by anhedral, homogeneous grains associated with synchysite-(Y) together as vein-filling phases, and is likely hydrothermal in origin coevally precipitated with synchysite-(Y).

316 Regarding the hydrothermal REE mineral assemblage, REE silicates represent the
317 earliest phase as these minerals were often crosscut by fluorite and synchysite-(Y).
318 Gadolinite-(Y), hingganite-(Y), and yttrialite-(Y) often occurred as veinlets crosscutting and
319 replacing feldspars and quartz, and in turn, being crosscut by veinlets of synchysite (Fig. 3d)
320 or pods of fluorite (Fig. 3e). Thus, both fluorite and synchysite post-dated these REE silicates.
321 For the fluorite and synchysite, Flr-1 and Flr-2 sometimes co-existed in the same mineral
322 grain, and when it happened, Flr-1 was either included as isolated patches in or crosscut by,
323 and embayed along contact by Flr-2 (Fig. 3g), suggesting that Flr-2 post-dated Flr-1.
324 Synchysite could be associated with Flr-2 as inclusions, and this indicates that synchysite
325 might precipitate slightly earlier than or co-precipitated with Flr-2. The synchysite inclusions
326 comprised synchysite-(Ce) that was crosscut, embayed, and penetrated by synchysite-(Y).
327 Moreover, synchysite-(Ce) only occurred in anhedral shape whereas some synchysite-(Y)
328 grains were large and subhedral to euhedral in shape (Figs. 6a & d), indicating synchysite-(Ce)
329 as an earlier phase pre-dating the crystallization of the synchysite-(Y).

330 The crosscutting relationship between zircon and synchysite (Fig. 6) suggested the
331 growth of Domain 4 was generally synchronous to synchysite-(Y), otherwise the corrosion
332 and embayment at the margin of the zircon grain would be expected as the fluid from which
333 the synchysite-(Y) precipitated should be F-rich and aggressive to zircon (Keppler, 1993).
334 From the petrographic examination, Domain 2 and 3 were likely to be generally coeval to the
335 precipitation of Flr-1 and/or replacement of Flr-1 by Flr-2, while Domain 4 to the
336 precipitation of synchysite-(Y) and/or replacement of synchysite-(Ce) by synchysite-(Y).

337

338 **5.2 Zircon archive of the magmatic-hydrothermal evolution**

339 Although zircon is generally regarded as a refractory mineral, it can be substantially
340 altered during metasomatism to form hydrothermal zircon (Ersay et al., 2022; Geisler et al.,

2003b; Soman et al., 2010; Wang et al., 2023; Yang et al., 2014). Hydrothermal zircon can form from alteration of magmatic zircon (e.g., Geisler et al., 2007 and references therein) and/ or direct precipitation from the hydrothermal fluids (e.g., Hoskin, 2005; Zhao et al., 2016). Morphology, structure, and chemical compositions of hydrothermal zircon grains are different from those of the magmatic counterparts, enabling an easy discrimination between the two (Fu et al., 2009). In Zudong granites, Domain 1 of zircon grains is transparent and shows bright CL and oscillatory growth zones (Fig. 4), indicating a well crystalline internal structure, which is further proved by the strong intensity and narrow, well-defined characteristic peaks in the Raman spectra (Fig. 5). The uniform chemical composition of Domain 1 with high Zr content and low Hf and other minor element contents is more commonly of magmatic origin (Hoskin and Schaltegger, 2003). All these suggest that Domain 1 crystallized from high temperature granitic magma (Pupin, 1980).

Domain 2 is murky, porous, and dark in CL (Fig. 4). Also, the lower intensity and boarder, less well-defined characteristic peaks in the Raman spectra (Fig. 5) suggest that this domain was highly metamict, with lower crystallinity due to radiation damage from decay of U and Th (Geisler et al., 2003a; Wang et al., 2014). The porous and inclusion-rich texture suggest that Domain 2 likely formed via a dissolution-reprecipitation process (Chen and Zhou, 2017; Geisler et al., 2007; Hay and Dempster, 2009; Tomaschek et al., 2003), very often during the interaction between metamict zircon and fluids (Geisler et al., 2007). Often, Domain 2 occurred in core of zircon grains or as overgrowth on Domain 1, suggesting its formation through interaction of Domain 1 with fluids. Domains 3 and 4 show transparent to slightly murky appearance, dark CL images, and occasionally, oscillatory growth zones (Fig. 4). Although zircon of dark CL with or without oscillatory growth zones can form from a volatile-rich residual melt at a late magmatic stage (Erdmann et al., 2013; Gagnevin et al., 2010; Kozlik et al., 2016), Domains 3 and 4 often occurred as overgrowth on Domain 2 (Figs.

4, 8 & 9), suggesting that they post-dated Domain 2 and more likely to have formed hydrothermally. In the Raman spectra, no characteristic peaks of zircon can be identified but only strong fluorescence (Fig. 5), suggesting a highly metamict and amorphous state. Metamictization-induced structural distortion facilitated significant incorporation of non-formula elements, such as the REE, Al, P, and Ca into the structure of zircon (Burnham, 2020; Geisler et al., 2003b). Alternatively, the elevated concentrations of these elements could be due to inclusions in the zircon grains (Burnham, 2020), but this explanation seems less likely in Zudong because of the positive correlation between REEs and Al concentrations in the zircon and the absence of any REE-Al-bearing inclusions of any observable size in the studied grains.

The incorporation of REE into zircon was very likely coupled with substitution of P through the reaction as $REE^{3+} + P^{5+} = Zr^{4+} + Si^{4+}$, as shown by positive correlations between P and REE of coefficients being 0.70 (Fig. 12a). Aluminum also shows positive correlation coefficient with REE (r^2 = 0.67; Fig. 12b). However, a coupled substitution of REE^{3+} and Al^{3+} for Zr^{4+} and Si^{4+} is not charge-balanced when Al^{3+} is shown to reside at the Si site of zircon (Claridge et al., 1994), while a coupled substitution of REE^{3+}, P^{5+} and Al^{3+} for Zr^{4+} and Si^{4+} is not site-balanced. Thus, it is likely that Al substituted through the reaction as $Al^{3+} + P^{5+} = 2Si^{4+}$, and the positive correlation between REE and Al could be coincidental related to the magmatic-hydrothermal fractionation of these elements. Substitution of non-formula elements into zircon is commonly attributed to increasing involvement of fluids (Geisler et al., 2007) and in amorphous metamict domains. In addition, the low analytical totals of these Domains, often attributed to the presence of molecular H_2O or OH in the structure (Nasdala et al., 2009), also indicate a volatile-oversaturated forming condition.

In Zudong, this process is supported by the progressive enrichment of Hf in zircon from Domains 1 to 5 (Figs. 7 - 9), consistent with a magmatic to hydrothermal transition

This is the peer-reviewed, final accepted version for American Mineralogist, published by the Mineralogical Society of America.
The published version is subject to change. Cite as Authors (Year) Title. American Mineralogist, in press.
DOI: https://doi.org/10.2138/am-2023-9117. http://www.minsocam.org/

because Hf is more incompatible than Zr during purely magmatic fractional crystallization and hence, tends to be enriched in the residual melt (Irber, 1999; Linnen and Keppler, 2002). Domains 2 to 4 of zircon likely formed under a volatile-oversaturated condition in the latest magmatic stage to magmatic-hydrothermal transition. Domain 5 signifies the final re-equilibration of the zircon with the fluid. The re-equilibration of Domain 5 was likely due to a diffusion-reaction process (Geisler et al., 2007) that produced irregular and inward-penetrating patchy reaction zones overprinting previous domains.

5.3 Fluid-mineral interaction and multiple mobilization of REEs

In hydrothermal systems, interactions of zircon with fluids under varying physicochemical conditions can be recorded in the textures and compositions of individual grains (Geisler et al., 2007; Hoskin, 2005). On the other hand, insight on the fluid chemistry can be shed from the mineral paragenetic sequence. The results obtained from these two sources can be applied to trace the evolution of the fluid.

In Zudong, the low concentrations of Sr and Eu, also the significant negative Eu anomalies and the tetrad REE pattern (Fig. 10b), attest to the highly evolved nature of the Zudong pluton, whereas the variable REE concentrations point to a metasomatic origin. The non-chondritic Y/Ho ratio (32.7 on average; compared to the chondritic Y/Ho ratio of 28; Bau (1996)), shows a strong enrichment of Y in the Zudong pluton, which also supports involvement of an aqueous fluid (Bau, 1996; Irber, 1999). Bulk geochemistry indicates that REE mineralization occurred under a F-rich, volatile-rich, and highly evolved (Rb-rich) conditions. From the mineral paragenesis, re-mobilization of the REE has taken place through reaction of the previously deposited REE-bearing minerals, including the dissolution of the REE silicates and primary REE phosphates and niobates, for instance the dissolution of

Gadolinite: $Y_2FeBe_2Si_2O_{10} + 12H^+ \rightarrow 2Y^{3+} + Fe^{2+} + 2Be^{2+} + 2H_4SiO_4 + 2H_2O$ (1)

Hingganite: $Y_2Be(SiO_4)_2(OH)_2 + 10H^+ \rightarrow 2Y^{3+} + 2Be^{2+} + 2H_4SiO_4 + 2H_2O$ (2)

Yttrialite-(Y): $Y_2Si_2O_7 + 6H^+ + H_2O \rightarrow 2Y^{3+} + 2H_4SiO_4$ (3)

Also, the fluid-mineral interaction promoted dissolution of the REE-enriched fluorite (Flr-1) and reprecipitated as the REE-depleted fluorite (Flr-2). During this process, and together with the reaction (1) to (3), REE, especially the HREE, would be re-mobilized by the fluid, that subsequently precipitated as REE-fluorocarbonate, whereas Be was likely lost to the fluid as there are no late Be-bearing minerals observed. Here, an acidic fluid is presumed to initiate the mineral dissolution, considering that the precipitation of hematite, through oxidation of Fe^{2+} liberated from the alteration of biotite, would generate H^+ in an oxidizing fluid through the reaction after Reed (1997):

$2Fe^{2+} + 0.5O_{2(aq)} + 2H_2O \rightarrow Fe_2O_3 + 4H^+$ (4)

From the petrographic examination, synchysite is the dominant REE-fluorocarbonate phase in the Zudong granite, of which synchysite-(Ce) precipitated first, was then replaced by synchysite-(Y) (Syn-1), and then locally further by HREE-enriched synchysite-(Y) (Syn-2). The precipitation of synchysite could be produced through the following as suggested by Ngwenya (1994):

$REECO_3F_{(aq)} + Ca^{2+} + HCO_3^- \rightarrow REECa(CO_3)_2F_{(s)} + H^+$ (5)

This suggests that the fluid was Ca-F-CO_2-REE-rich, also implied by the high F and CO_2 content of the granites (Table S3), and particularly Ca-rich throughout the entire mineralization for the absence of bastnäsite or parisite precipitation, that often takes place after synchysite (Förster, 2001; Ngwenya, 1994). Moreover, the fluid would have become slightly HREE-enriched in the final stage to locally replace Syn-1 with Syn-2. Considering the pH buffering ability of the major minerals, notably feldspar and quartz, is low, the consumed H^+ for mineral dissolution (e.g., Reaction 1 to 3) could be replenished by the H^+ produced from Reaction 4 until either REE^{3+}, HCO_3^- or F^- has been exhausted by the

441 precipitation of synchysite. The paragenetic sequence of the REE-bearing minerals is
442 summarized in Fig. 13a.

443 The evolution trajectory is recorded in the zircon (Fig. 13). For instance, the coupled
444 dissolution-reprecipitation (CDP) of zircon that formed the growth zone of Domain 2
445 typically involves dissolution by a F-rich fluid (Keppler, 1993), after which the mobilized
446 REE were redistributed in a highly uneven REE enrichment, whereas the repeated truncation
447 of the porous domain by a later clean, inclusion-free domain (Domain 3) reflects fluctuating
448 fluid chemistry between Zr under-saturation and over-saturation. This also points to a
449 fluctuation of the pH and F activity of the fluid, as zircon can be effectively dissolved in
450 acidic, F-bearing fluid (Keppler, 1993). Particularly when zircon is commonly spatially
451 associated with fluorite in the Zudong granite, the CDP of fluorite (replacement of Flr-1 by
452 Flr-2) would cause local fluctuation of the F activity of the fluid to motivate the CDP of
453 zircon (e.g., Han et al., 2019). The repeated re-mobilization of REE through CDP of zircon
454 would cause the significant REE enrichment in the Domain 3 and relative REE depletion in
455 the Domain 2 (Figs. 7 – 9; S2 – S4). After the CDP of the fluorite ended, F activity of the
456 fluid likely became steady and gradually decreased afterwards due to the precipitation of
457 synchysite. The consumption of fluoride in the fluid is manifested by the continuous growth
458 of the Domain 4 commonly rimming the Domain 2 and 3 and rarely being embayed and
459 corroded along the grain boundary. The final minor HREE metasomatism on the Syn-1 would
460 have coevally caused the HREE enrichment in the Domain 5 (Figs. 9; S2 – S4) through a
461 diffusion-reaction process. On the other hand, the progressive preferential enrichment of the
462 LREEs in the zircon [indicated by $(La/Yb)_N$ value; Table S2] implies that the fluid was also
463 progressively enriched in the LREE, consistent with previous experimental results showing
464 that mobility of the LREE is higher than the HREE (Migdisov et al., 2016). In this regard, the
465 exhaustion of fluoride would possibly be a key reason for the termination of REE

466 mineralization in the Zudong granite. To summarize, as a refractory phase capable at the
467 same time of being highly altered during metasomatism, the texture and composition of
468 zircon may record the evolution of the hydrothermal system and provide further insight to the
469 REE mineralization.

470 The combined mineralogical and geochemical records show that repetitive dissolution
471 and precipitation of REE-bearing minerals took place during the hydrothermal alteration of
472 the Zudong granites. Repeated mobilization and re-distribution caused progressive
473 enrichment and fractionation of the REE.

474

475 **5.4 Ce and Eu anomalies in zircon as indicator for fluid redox**

476 As Ce^{4+} can more readily substitute for Zr^{4+} than Ce^{3+}, magmatic zircon often shows a
477 positive Ce anomaly. The magnitude of the anomaly is demonstrated to increase with
478 increasing oxygen fugacity of the melt (cf. Trail et al., 2012), while the negative Eu anomaly
479 shown on the chondrite-normalized pattern is attributed to preferential incorporation of Eu^{2+}
480 in plagioclase prior to or during the crystallization of zircon (Hoskin and Schaltegger, 2003).
481 In zircons of the Zudong granites, the magmatic Domain 1 show typical positive Ce anomaly
482 and negative Eu anomaly (Fig. 10a). However, the Ce anomaly decreases from 49.6 on
483 average for the magmatic Domain 1 to ~2 in the hydrothermal Domains 2 to 4. In the final
484 phase, Domain 5, the average is 1.0, including some spots with negative anomalies (Fig. 10a).
485 This suggests the fluid was comparatively reducing during the HREE mineralization, that is
486 also supported by the negative correlation between the bulk REE concentration and
487 magnitude of Ce anomaly (Fig. 11e). The reducing condition could be attributed to the
488 precipitation of hematite prior to and throughout HREE mineralization that consumed O_2 in
489 the fluid. Synchronously, part of the Ce was likely oxidized to Ce^{4+} and decoupled from the
490 other REE. The reducing condition is also implied by variation of the Eu anomaly from 0.1

491 on average for Domain 1 to 0.01 on average for Domains 2 to 4 and 0.008 on average for
492 Domain 5 (Table S2). As Eu^{2+} is unlikely to substitute Zr^{4+} on the basis of cation charge and
493 size (cf. Trail et al., 2012), a more reducing condition would lead to greater depletion of Eu in
494 zircon, as manifested by the increasing negative Eu anomalies (Fig. 10a).
495
496 **6. Implications for HREE mineralization and REE fractionation in granitic systems**
497 The Zudong granites have very high HREE concentration and are favorable for
498 regolith-hosted ore formation during weathering (Li et al., 2019), and the HREE enrichment
499 is associated with intensifying REE fractionation, as shown by the negative correlation
500 between the bulk REE concentration and $(La/Yb)_N$ ratio (Fig. 11f). Hydrothermal alteration is
501 commonly thought to be the key process in boosting the HREE concentration of the granite
502 (Fan et al., 2023; Huang et al., 1989; Li et al., 2017). The source of the fluid and HREE is
503 most commonly attributed to either internally derivation from the granitic magma (Huang et
504 al., 1989) or from external sources, for instance subducted sediments (Fan et al., 2023). In
505 this study, petrographic and mineralogical examination of the REE-bearing minerals,
506 particularly zircon, reveals that multiple stages of mobilization of the REE happened during
507 hydrothermal alteration. A significant amount of the major and mobile elements would be
508 removed in this process, likewise for the LREE. Temperature of the REE mineralization was
509 likely close to magmatic as suggested by the coexistence of fluorite and REE-
510 fluorocarbonates (Williams-Jones and Wood, 1992). A study of a similar style of alteration at
511 the Erzgebirge district suggested a maximum mineralization temperature of 550 - 600°C
512 (Förster, 2001). Light REE would be highly mobilized through Cl complexation in this
513 temperature range (Migdisov et al., 2016; Williams-Jones et al., 2012), and hence
514 preferentially lost to the exsolved fluid (Bau and Dulski, 1995), resulting in the observed

LREE depletion in Zudong granites. In contrast, the HREE were enriched through the extensive mineralization of synchysite-(Y).

This study showcases that, apart from a HREE-rich fluid (cf. Fan et al., 2023), multiple stages of mobilization of the HREE during the hydrothermal alteration is essential in upgrading the HREE concentrations to an ore grade or a sub-ore grade that could facilitate the formation of regolith-hosted HREE deposits subsequently during weathering. In this process, repeated mineral dissolution and (re)precipitation of the REE-bearing minerals would progressively fractionate the REE, with the LREE being mobilized and the HREE extensively mineralizing as the newly precipitated mineral phases. At the same time, the process would cause substantial dissolution of the major minerals, like feldspars and micas, resulting in a net decrease in the major element contents with consequent increase in the bulk HREE content of the altered rocks.

Acknowledgements

We thank Ms Xiao Fu for the support on XRF and EPMA analyses. Editorial handling and comments by Associate Editor Dr. Paul Tomascak, and constructive reviews0 by Dr. El Saeed R. Lasheen and an anonymous reviewer are very much appreciated. This study was supported financially by the Natural Science Foundation of China (Grant No. 92162323, 91962216) and the Guangdong Basic and Applied Basic Research Foundation (Grant No. 2021A1515011524) to M.-F.Z.

Appendix A. Supplementary Material

Supplementary Information: Figure S1 – S6, EDS spectra of synchysite

Supplementary Table: Table S1 – S3

References

Anenburg, M., and Williams, M.J. (2022) Quantifying the tetrad effect, shape components, and Ce–Eu–Gd anomalies in rare earth element patterns. Mathematical Geosciences, 54(1), 47-70.

Bau, M. (1996) Controls on the fractionation of isovalent trace elements in magmatic and aqueous systems: evidence from Y/Ho, Zr/Hf, and lanthanide tetrad effect. Contributions to Mineralogy and Petrology, 123(3), 323-333.

Bau, M., and Dulski, P. (1995) Comparative study of yttrium and rare-earth element behaviours in fluorine-rich hydrothermal fluids. Contributions to Mineralogy and Petrology, 119(2), 213-223.

Bea, F. (1996) Residence of REE, Y, Th and U in granites and crustal protoliths; implications for the chemistry of crustal melts. Journal of petrology, 37(3), 521-552.

Bea, F., Pereira, M., Corretgé, L., and Fershtater, G. (1994) Differentiation of strongly peraluminous, perphosphorus granites: the Pedrobernardo pluton, central Spain. Geochimica et Cosmochimica Acta, 58(12), 2609-2627.

Breiter, K., Frýda, J., Seltmann, R., and Thomas, R. (1997) Mineralogical evidence for two magmatic stages in the evolution of an extremely fractionated P-rich rare-metal granite: the Podlesí stock, Krušné hory, Czech Republic. Journal of Petrology, 38(12), 1723-1739.

Burnham, A.D. (2020) Key concepts in interpreting the concentrations of the rare earth elements in zircon. Chemical Geology, 551, 119765.

Chen, W.T., and Zhou, M.-F. (2017) Hydrothermal alteration of magmatic zircon related to NaCl-rich brines: Diffusion-reaction and dissolution-reprecipitation processes. American Journal of Science, 317(2), 177-215.

564 Claridge, R., Mackle, K., Sutton, G., and Tennant, W. (1994) 10 K EPR of an oxygen-hole
565 aluminium centre, $[AlO_4]_0$, in X-irradiated zircon, $ZrSiO_4$. Journal of Physics:
566 Condensed Matter, 6(47), 10415-10422.
567 Eby, G.N. (1990) The A-type granitoids: a review of their occurrence and chemical
568 characteristics and speculations on their petrogenesis. Lithos, 26(1), 115-134.
569 Erdmann, S., Wodicka, N., Jackson, S., and Corrigan, D. (2013) Zircon textures and
570 composition: refractory recorders of magmatic volatile evolution? Contributions to
571 Mineralogy and Petrology, 165, 45-71.
572 Ersay, L., Greenough, J.D., Larson, K.P., and Dostal, J. (2022) Zircon reveals multistage,
573 magmatic and hydrothermal Rare Earth Element mineralization at Debert Lake, Nova
574 Scotia, Canada. Ore Geology Reviews, 144, 104780.
575 Fan, C., Xu, C., Shi, A., Smith, M.P., Kynicky, J., and Wei, C. (2023) Origin of heavy rare
576 earth elements in highly fractionated peraluminous granites. Geochimica et
577 Cosmochimica Acta, 343, 371-383.
578 Förster, H.-J. (2001) Synchysite-(Y)–synchysite-(Ce) solid solutions from Markersbach,
579 Erzgebirge, Germany: REE and Th mobility during high-T alteration of highly
580 fractionated aluminous A-type granites. Mineralogy and Petrology, 72(4), 259-280.
581 Fu, B., Mernagh, T.P., Kita, N.T., Kemp, A.I., and Valley, J.W. (2009) Distinguishing
582 magmatic zircon from hydrothermal zircon: a case study from the Gidginbung high-
583 sulphidation Au–Ag–(Cu) deposit, SE Australia. Chemical Geology, 259(3-4), 131-
584 142.
585 Gagnevin, D., Daly, J.S., and Kronz, A. (2010) Zircon texture and chemical composition as a
586 guide to magmatic processes and mixing in a granitic environment and coeval
587 volcanic system. Contributions to Mineralogy and Petrology, 159, 579-596.

588 Geisler, T., Pidgeon, R.T., Kurtz, R., Van Bronswijk, W., and Schleicher, H. (2003a)
589 Experimental hydrothermal alteration of partially metamict zircon. American
590 Mineralogist, 88(10), 1496-1513.
591 Geisler, T., Rashwan, A., Rahn, M., Poller, U., Zwingmann, H., Pidgeon, R., Schleicher, H.,
592 and Tomaschek, F. (2003b) Low-temperature hydrothermal alteration of natural
593 metamict zircons from the Eastern Desert, Egypt. Mineralogical Magazine, 67(3),
594 485-508.
595 Geisler, T., Schaltegger, U., and Tomaschek, F. (2007) Re-equilibration of zircon in aqueous
596 fluids and melts. Elements, 3(1), 43-50.
597 Han, J., Chen, H., Hollings, P., Jiang, H., Xu, H., Zhang, L., Xiao, B., Xing, C., and Tan, Z.
598 (2019) The formation of modified zircons in F-rich highly-evolved granites: An
599 example from the Shuangji granites in Eastern Tianshan, China. Lithos, 324, 776-788.
600 Hanchar, J.M., and Van Westrenen, W. (2007) Rare earth element behavior in zircon-melt
601 systems. Elements, 3(1), 37-42.
602 Hay, D., and Dempster, T. (2009) Zircon behaviour during low-temperature metamorphism.
603 Journal of Petrology, 50(4), 571-589.
604 Henderson, P. (2013) Rare earth element geochemistry. Elsevier.
605 Hoskin, P.W. (2005) Trace-element composition of hydrothermal zircon and the alteration of
606 Hadean zircon from the Jack Hills, Australia. Geochimica et Cosmochimica Acta,
607 69(3), 637-648.
608 Hoskin, P.W., and Schaltegger, U. (2003) The composition of zircon and igneous and
609 metamorphic petrogenesis. Reviews in mineralogy and geochemistry, 53(1), 27-62.
610 Huang, D., Wu, C., and Han, J. (1989) REE geochemistry and mineralization characteristics
611 of the Zudong and Guanxi granites, Jiangxi Province. Acta Geologica Sinica (English
612 edition), 2(2), 139-157.

Irber, W. (1999) The lanthanide tetrad effect and its correlation with K/Rb, Eu/Eu∗, Sr/Eu, Y/Ho, and Zr/Hf of evolving peraluminous granite suites. Geochimica et Cosmochimica Acta, 63(3-4), 489-508.

Keppler, H. (1993) Influence of fluorine on the enrichment of high field strength trace elements in granitic rocks. Contributions to Mineralogy and Petrology, 114(4), 479-488.

Kozlik, M., Raith, J.G., and Gerdes, A. (2016) U–Pb, Lu–Hf and trace element characteristics of zircon from the Felbertal scheelite deposit (Austria): New constraints on timing and source of W mineralization. Chemical Geology, 421, 112-126.

Li, M.Y.H., Zhou, M.-F., and Williams-Jones, A.E. (2019) The genesis of regolith-hosted heavy rare earth element deposits: Insights from the world-class Zudong deposit in Jiangxi Province, South China. Economic Geology, 114(3), 541-568.

Li, Y.H.M., Zhao, W.W., and Zhou, M.-F. (2017) Nature of parent rocks, mineralization styles and ore genesis of regolith-hosted REE deposits in South China: An integrated genetic model. Journal of Asian Earth Sciences, 148, 65-95.

Linnen, R.L., and Keppler, H. (2002) Melt composition control of Zr/Hf fractionation in magmatic processes. Geochimica et Cosmochimica Acta, 66(18), 3293-3301.

Migdisov, A., Williams-Jones, A., Brugger, J., and Caporuscio, F.A. (2016) Hydrothermal transport, deposition, and fractionation of the REE: Experimental data and thermodynamic calculations. Chemical Geology, 439, 13-42.

Nasdala, L., Kronz, A., Wirth, R., Váczi, T., Perez-Soba, C., Willner, A., and Kennedy, A.K. (2009) The phenomenon of deficient electron microprobe totals in radiation-damaged and altered zircon. Geochimica et Cosmochimica Acta, 73(6), 1637-1650.

636 Ngwenya, B.T. (1994) Hydrothermal rare earth mineralisation in carbonatites of the Tundulu
637 complex, Malawi: Processes at the fluid/rock interface. Geochimica et Cosmochimica
638 Acta, 58(9), 2061-2072.
639 Pupin, J. (1980) Zircon and granite petrology. Contributions to Mineralogy and Petrology,
640 73(3), 207-220.
641 Reed, M.H. (1997) Hydrothermal alteration and its relationship to ore fluid composition. In H.
642 Barnes, Ed. Geochemistry of hydrothermal ore deposits, p. 303-366. John Wileys &
643 Sons, Inc., Canada.
644 Sanematsu, K., and Watanabe, Y. (2016) Characteristics and genesis of ion-adsorption type
645 deposits. Reviews in Economic Geology, 18, 55-79.
646 Sarbas, B. (2008) The GEOROC database as part of a growing geoinformatics network.
647 Geoinformatics 2008—Data to Knowledge, p. 42-43. USGS.
648 Schneider, D., Bachtel, J., and Schmitt, A. (2012) Zircon alteration in wall rock of Pamour
649 and Hoyle Pond Au deposits, Abitibi greenstone belt: Constraints on timescales of
650 fluid flow from depth-profiling techniques. Economic Geology, 107(5), 1043-1072.
651 Soman, A., Geisler, T., Tomaschek, F., Grange, M., and Berndt, J. (2010) Alteration of
652 crystalline zircon solid solutions: a case study on zircon from an alkaline pegmatite
653 from Zomba–Malosa, Malawi. Contributions to Mineralogy and Petrology, 160, 909-
654 930.
655 Tomaschek, F., Kennedy, A.K., Villa, I.M., Lagos, M., and Ballhaus, C. (2003) Zircons from
656 Syros, Cyclades, Greece—recrystallization and mobilization of zircon during high-
657 pressure metamorphism. Journal of Petrology, 44(11), 1977-2002.
658 Trail, D., Watson, E.B., and Tailby, N.D. (2012) Ce and Eu anomalies in zircon as proxies for
659 the oxidation state of magmas. Geochimica et Cosmochimica Acta, 97, 70-87.
660 U.S. Geological Survey. (2023) Mineral commodity summaries 2023, p. 210.

661 Vasyukova, O., and Williams-Jones, A. (2018) Direct measurement of metal concentrations
662 in fluid inclusions, a tale of hydrothermal alteration and REE ore formation from
663 Strange Lake, Canada. Chemical Geology, 483, 385-396.
664 Verplanck, P., Mariano, A., and Mariano Jr, A. (2016) Rare earth element ore geology of
665 carbonatites. Reviews in Economic Geology, 18, 5-32.
666 Wang, H., He, H., Yang, W., Bao, Z., Liang, X., Zhu, J., Ma, L., and Huang, Y. (2023)
667 Zircon texture and composition fingerprint HREE enrichment in muscovite granite
668 bedrock of the Dabu ion-adsorption REE deposit, South China. Chemical Geology,
669 616, 121231.
670 Wang, X.-L., Coble, M.A., Valley, J.W., Shu, X.-J., Kitajima, K., Spicuzza, M.J., and Sun, T.
671 (2014) Influence of radiation damage on Late Jurassic zircon from southern China:
672 Evidence from in situ measurements of oxygen isotopes, laser Raman, U–Pb ages,
673 and trace elements. Chemical Geology, 389, 122-136.
674 Williams-Jones, A.E., Migdisov, A.A., and Samson, I.M. (2012) Hydrothermal mobilisation
675 of the rare earth elements–a tale of “ceria” and “yttria”. Elements, 8(5), 355-360.
676 Williams-Jones, A.E., Samson, I.M., and Olivo, G.R. (2000) The genesis of hydrothermal
677 fluorite-REE deposits in the Gallinas Mountains, New Mexico. Economic Geology,
678 95(2), 327-341.
679 Williams-Jones, A.E., and Wood, S.A. (1992) A preliminary petrogenetic grid for REE
680 fluorocarbonates and associated minerals. Geochimica et Cosmochimica Acta, 56(2),
681 725-738.
682 Xu, C., Kynický, J., Smith, M.P., Kopriva, A., Brtnický, M., Urubek, T., Yang, Y., Zhao, Z.,
683 He, C., and Song, W. (2017) Origin of heavy rare earth mineralization in South China.
684 Nature Communications, 8, 14598.

685 Yang, W.-B., Niu, H.-C., Shan, Q., Sun, W.-D., Zhang, H., Li, N.-B., Jiang, Y.-H., and Yu,
686 X.-Y. (2014) Geochemistry of magmatic and hydrothermal zircon from the highly
687 evolved Baerzhe alkaline granite: implications for Zr–REE–Nb mineralization.
688 Mineralium Deposita, 49(4), 451-470.
689 Zeng, L.-J., Niu, H.-C., Bao, Z.-W., and Yang, W.-B. (2017) Chemical lattice expansion of
690 natural zircon during the magmatic-hydrothermal evolution of A-type granite.
691 American Mineralogist, 102(3), 655-665.
692 Zhao, W.W., Zhou, M.-F., and Chen, W.T. (2016) Growth of hydrothermal baddeleyite and
693 zircon in different stages of skarnization. American Mineralogist, 101(12), 2689-2700.
694 Zhao, Z., Wang, D., Chen, Z., Chen, Z., Zhwng, G., and Liu, X. (2014) Zircon U-Pb age,
695 endogenic mineralization and petrogenesis of rare earth ore-bearing granite in
696 Longnan, Jiangxi province. Acta Geoscientica sinica, 35(6), 719-725.
697 Zhou, X., Sun, T., Shen, W., Shu, L., and Niu, Y. (2006) Petrogenesis of Mesozoic granitoids
698 and volcanic rocks in South China: A response to tectonic evolution. Episodes, 29(1),
699 26.

700

701

Figure captions

Figure 1. Simplified geological map of the Zudong pluton (after Li et al., 2019).

Figure 2. (a) A representative hand specimen of the Zudong granites showing the major mineral assemblage of quartz + feldspar + muscovite + hematite. (b) – (d) Cross-polarised light photomicrographs of the Zudong granites. (b) Alteration of albite by muscovite along cleavage plane. (c) Pseudomorph of muscovite + hematite after biotite. (d) Alteration of albite by hematite along the cleavage planes. Abbreviations: Ab = Albite; Fsp = K-Feldspar; Hem = Hematite; Ms = Muscovite; Qz = Quartz.

Figure 3. BSE images of the occurrence of the REE-bearing minerals in the Zudong granites. (a) Association of gadolinite-(Y) and yttrialite-(Y) in voids of albite. (b) Hingganite-(Y) replacing albite in a mesh of veinlet. (c) A hingganite-(Y)-calcite veinlet crosscutting K-feldspar. (d) Hingganite-(Y) being cut by synchysite-(Y). (e) Hingganite-(Y) veinlets being cut by fluorite. (f) A fluorite grain interstitial to muscovite and containing inclusions of synchysite. (g) REE-enriched fluorite (Flr-1) being replaced by REE-depleted fluorite (Flr-2) with synchysite inclusions. (h) & (i) Inclusions of synchysite-(Ce) in fluorite being replaced by synchysite-(Y). (j) Synchysite-(Ce) being replaced by synchysite-(Y) [Syn-1] and in turn being cut by HREE-enriched synchysite-(Y) [Syn-2]. Relict magmatic grain of (k) xenotime-(Y) and (l) fergusonite-(Y) showing oscillatory zoning. Abbreviations: Ab = Albite; Cal = Calcite; Fgs-Y = Fergusonite-(Y); Flr-1 = REE-enriched fluorite; Flr-2 = REE-depleted fluorite; Gad-Y = Gadonlite-(Y); Hin-Y = Hingganite-(Y); Fsp = K-feldspar; Syn = mixture of both synchysite-(Ce) and -(Y); Syn-Ce = Synchysite-(Ce); Syn-1 = Synchysite-(Y); Syn-2 = HREE-enriched Synchysite-(Y); Xtm-Y = Xenotime-(Y); Ytt-Y = Yttrialite-(Y).

727

728 **Figure 4**. Occurrence of zircon of different domains. Scale bars indicate a length of 100 μm.
729 Abbreviations: Tr = image under transmitted light, BSE = BSE image, CL = CL image.

730

731 **Figure 5**. Representative Raman spectra of different domains of zircon in the Zudong
732 granites.

733

734 **Figure 6**. BSE images of the association of zircon with other REE-bearing minerals in the
735 Zudong granites. (a) An inclusion of zircon in synchysite-(Y). (b) A close up of the zircon
736 grain in (a) showing a porous Domain 2 rimmed by a broad continuous growth zone (Domain
737 4); Domain 4 is not embayed by the synchysite-(Ce) and locally overgrown by xenotime-(Y).
738 (c) Zircon grains included in fluorite and associated with synchysite; porous relict grains
739 (Domain 2) are connected by subsequent hydrothermal growth (Domain 4) that cut a grain of
740 Th-bearing synchysite-(Ce). (d) Zircon grain corroded and overgrown by synchysite-(Y)
741 [Syn-1]. (e) A relict zircon grain (Domain 1?) embayed by the growth of synchysite-(Ce)
742 along the margin. (f) Partial dissolution of a zircon grain in fluorite. Abbreviations: Zrn =
743 Zircon; other abbreviations are the same to those in Figure 3.

744

745 **Figure 7**. Variations of elemental contents in different domains of zircon in the Zudong
746 granites. The minimum and maximum of the box and whisker plots are defined based on the
747 1.5 × IQR (interquartile range) value, with the minimum at Q1 – 1.5 × IQR and maximum at
748 Q3 + 1.5 × IQR. Q1 and Q3 are the 25^{th} and 75^{th} percentiles, respectively.

749

750 **Figure 8**. Images and elemental compositions of a representative zircon grain in the Zudong
751 granites.

752

753 **Figure 9**. Images and variations in elemental compositions of representative zircon grains in
754 the Zudong granites.

755

756 **Figure 10**. Chondrite-normalized REE patterns of (a) different domains of zircon and (b) the
757 whole-rock REE concentration of the Zudong granites.

758

759 **Figure 11**. Bivariant correlations between the whole-rock REE concentrations and selected
760 elements and elemental ratios.

761

762 **Figure 12**. Correlations between REE concentrations and (a) Al and (b) P for different
763 domains of zircon in the Zudong granites.

764

765 **Figure 13**. (a) Interpretations of the paragenetic sequence of the REE-bearing minerals in
766 Zudong granites and (b) the evolution of zircon recording the mineral-fluid interaction for the
767 HREE mineralization.

768

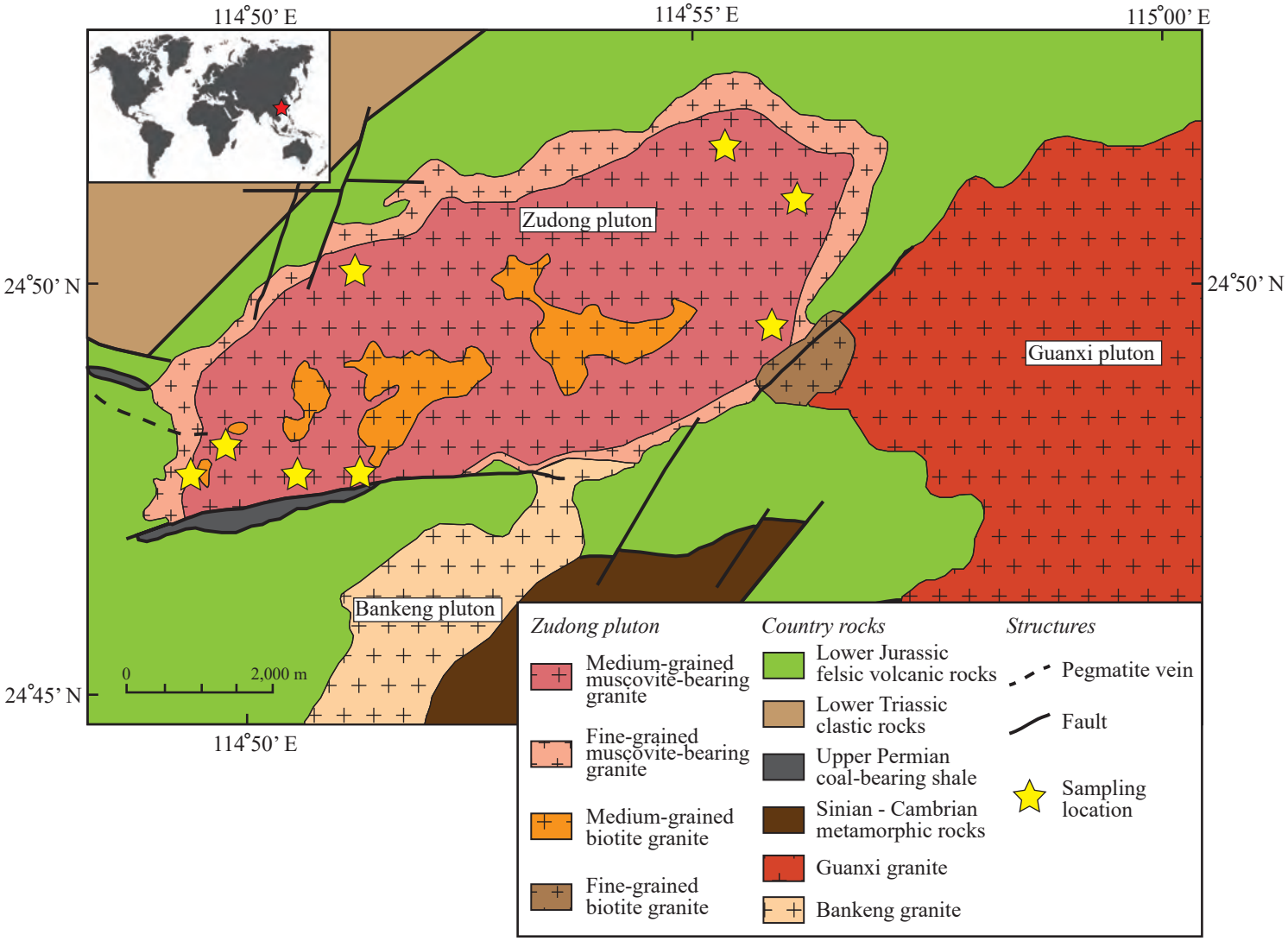

Figure 1

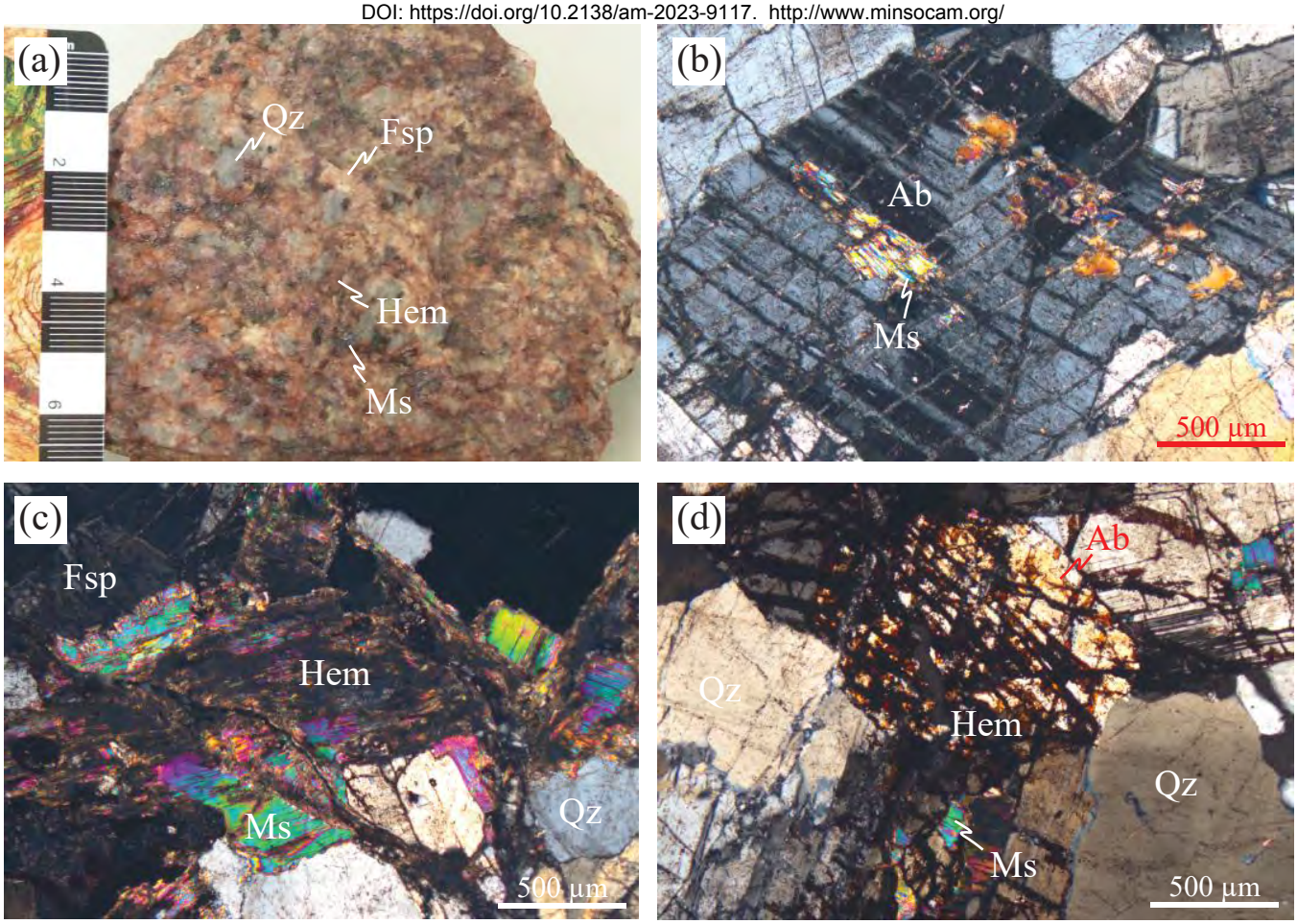

Figure 2

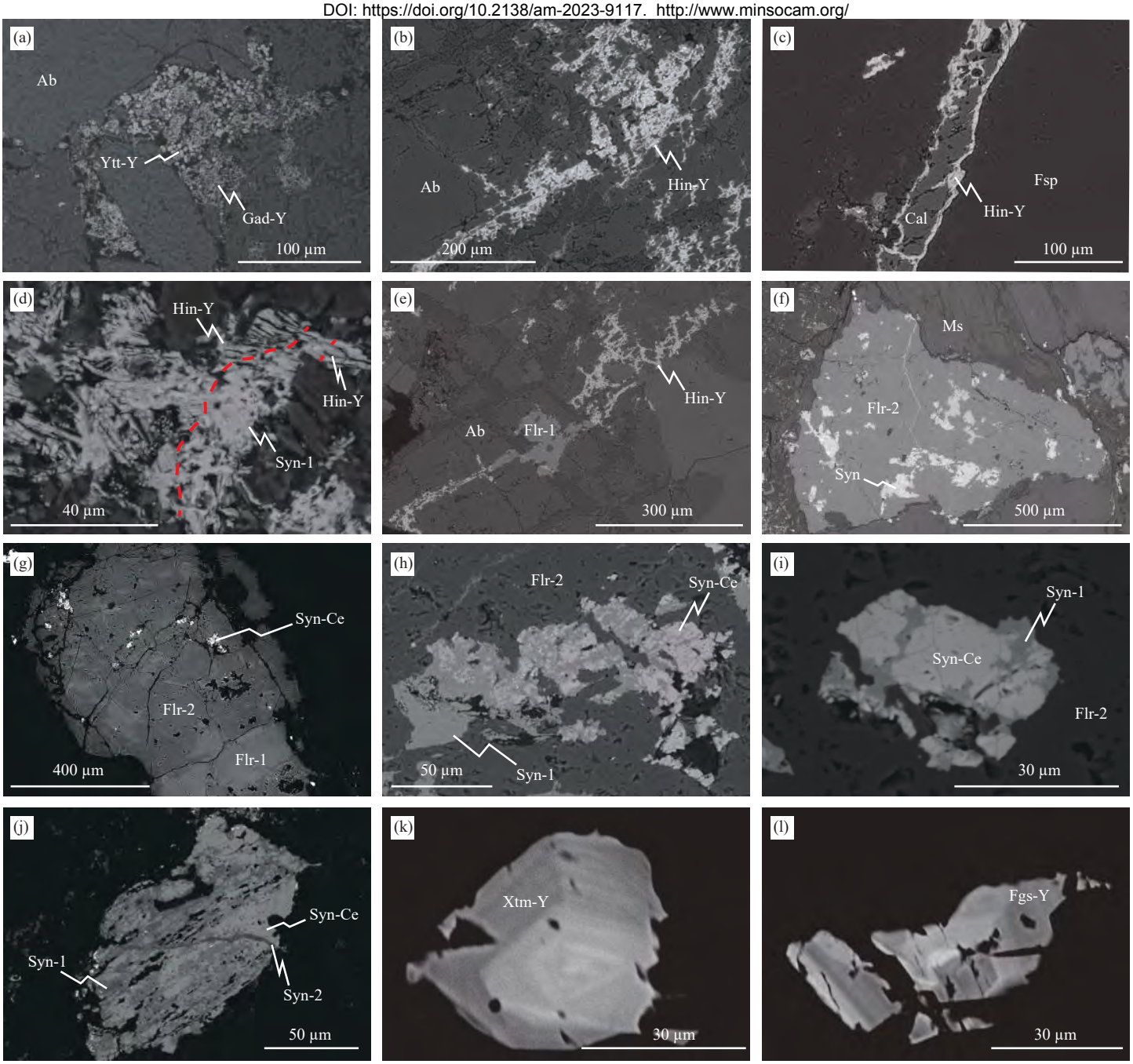

Figure 3

This is the peer-reviewed, final accepted version for American Mineralogist, published by the Mineralogical Society of America.
The published version is subject to change. Cite as Authors (Year) Title. American Mineralogist, in press.
DOI: https://doi.org/10.2138/am-2023-9117. http://www.minsocam.org/

(a) Domain 1

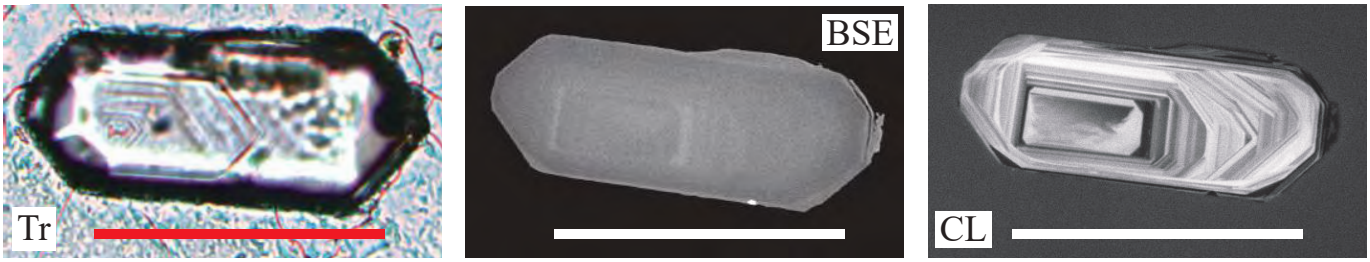

(b) Domain 2 & 3

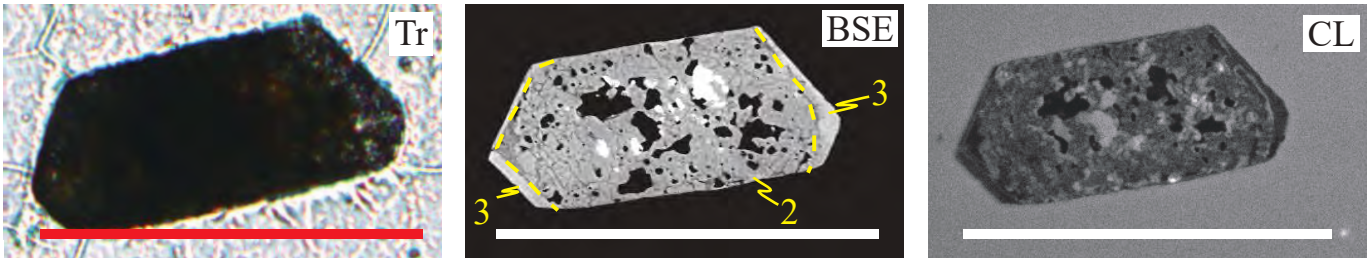

(c) Domain 2 - 5

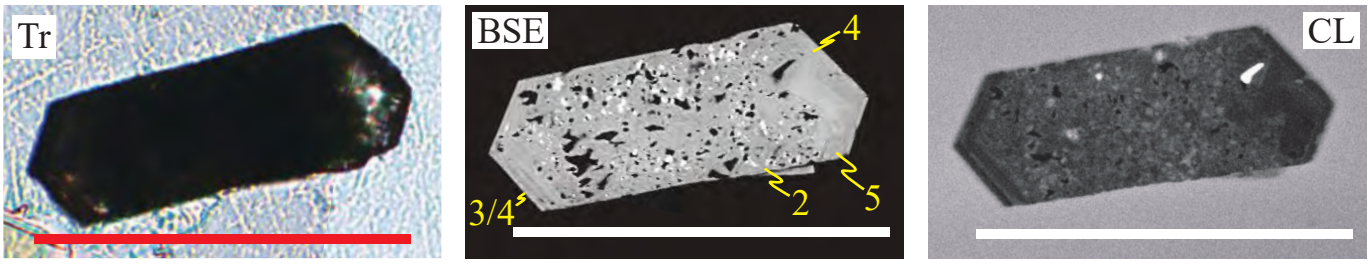

(d) Domain 4 & 5

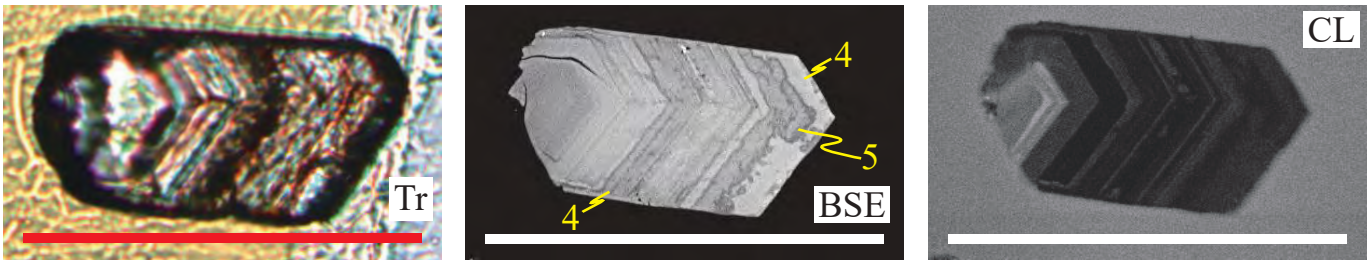

Figure 4

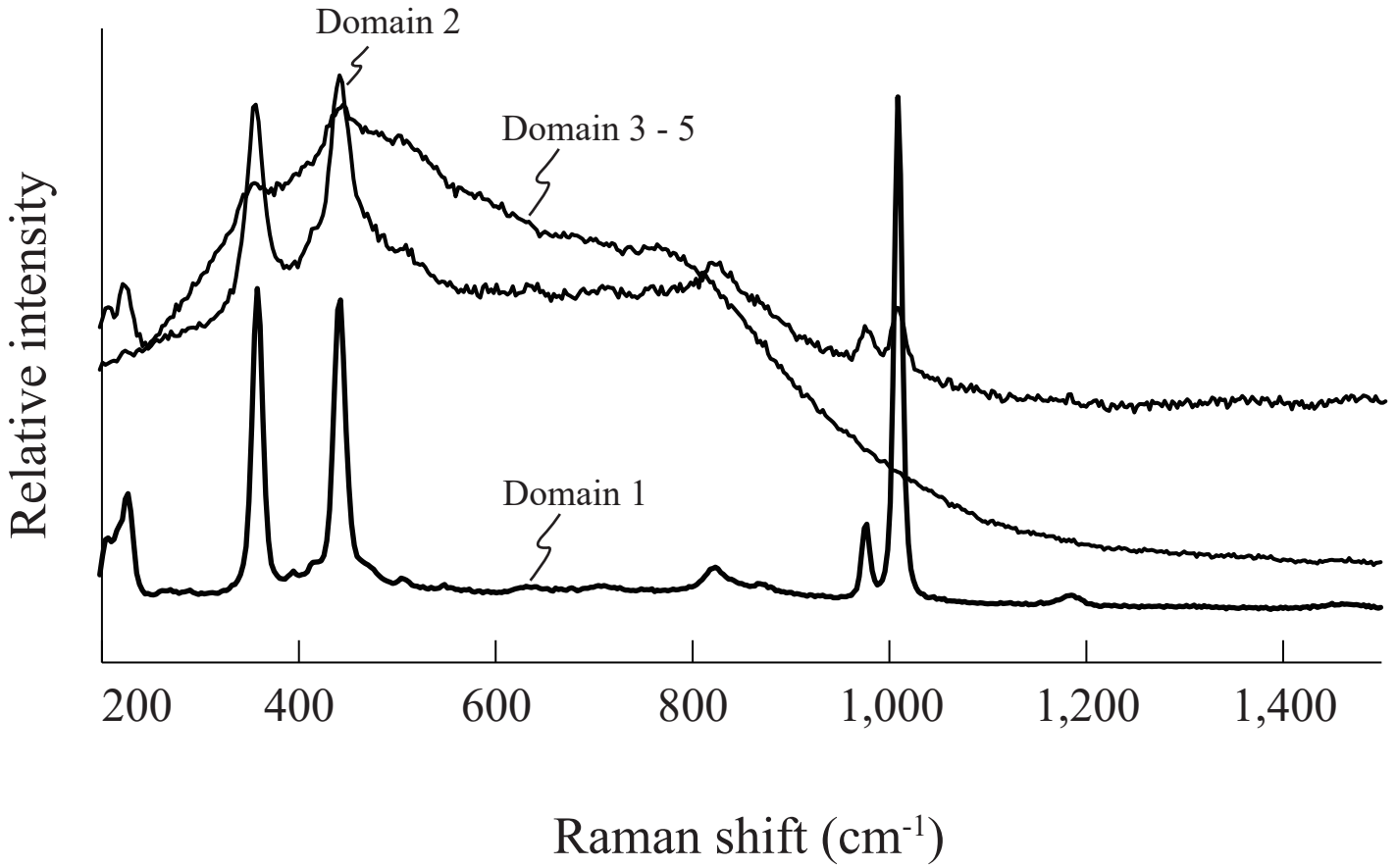

Figure 5

This is the peer-reviewed, final accepted version for American Mineralogist, published by the Mineralogical Society of America.
The published version is subject to change. Cite as Authors (Year) Title. American Mineralogist, in press.
DOI: https://doi.org/10.2138/am-2023-9117. http://www.minsocam.org/

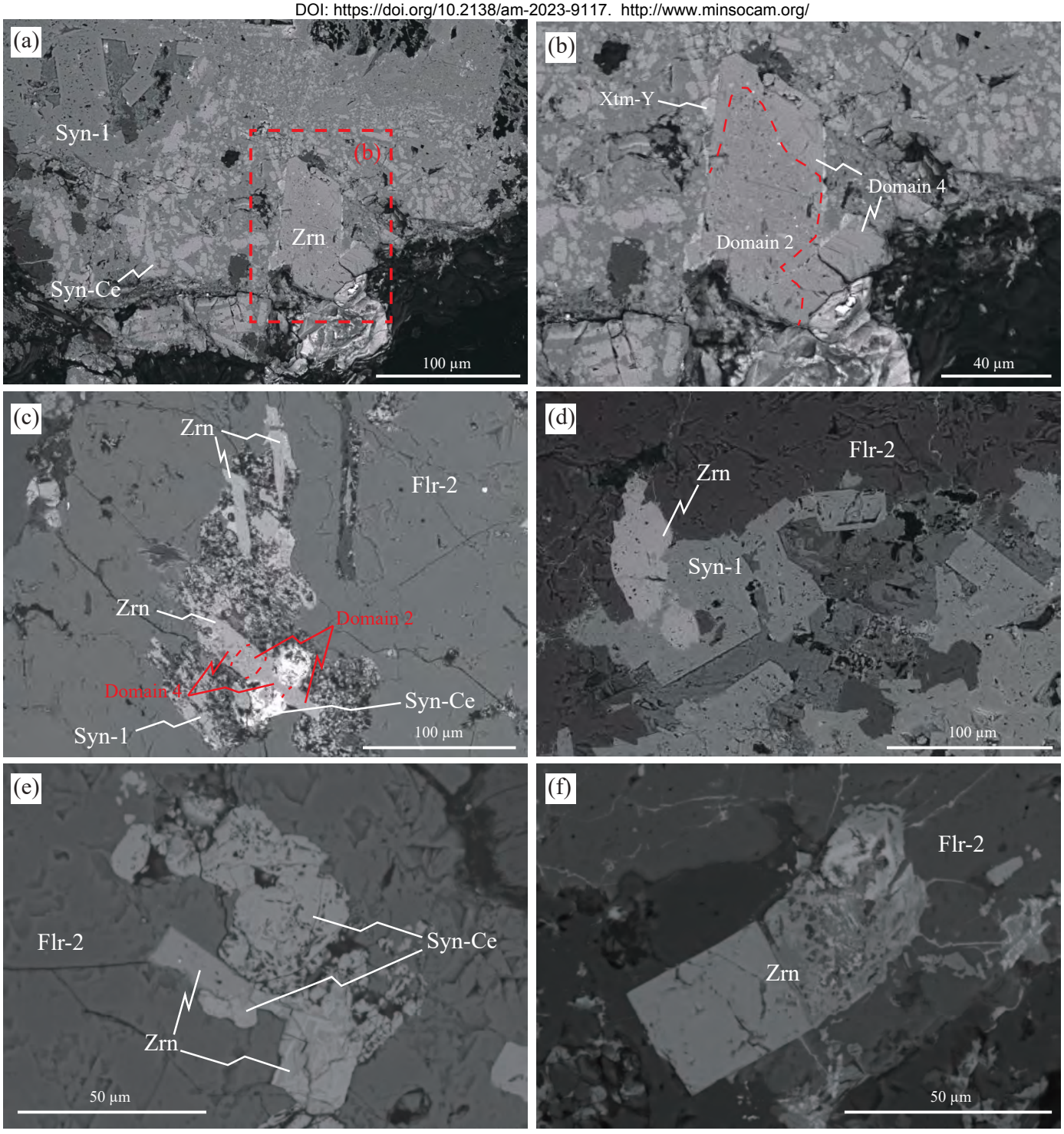

Figure 6

This is the peer-reviewed, final accepted version for American Mineralogist, published by the Mineralogical Society of America.
The published version is subject to change. Cite as Authors (Year) Title. American Mineralogist, in press.
DOI: https://doi.org/10.2138/am-2023-9117. http://www.minsocam.org/

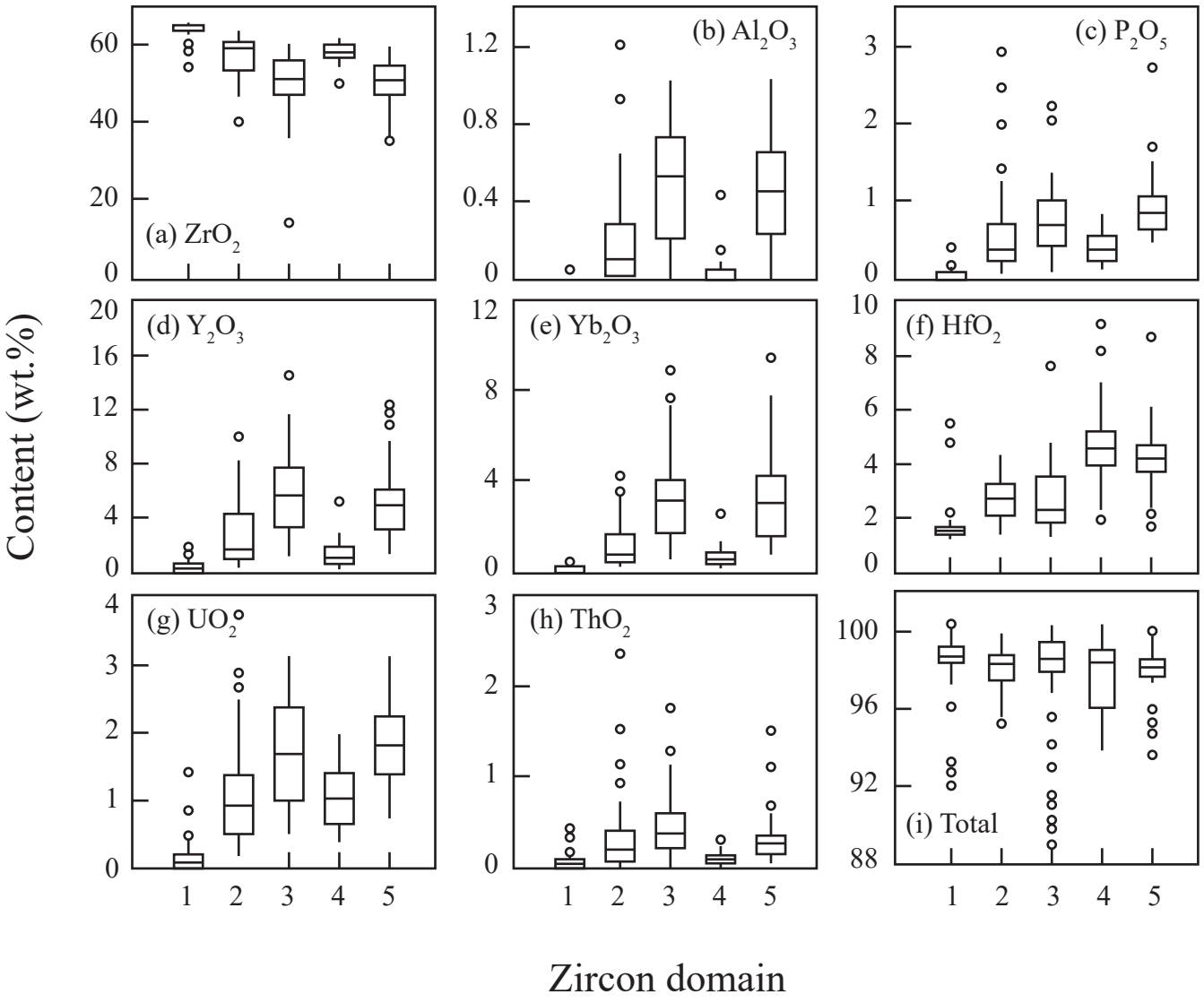

Figure 7

This is the peer-reviewed, final accepted version for American Mineralogist, published by the Mineralogical Society of America.
The published version is subject to change. Cite as Authors (Year) Title. American Mineralogist, in press.
DOI: https://doi.org/10.2138/am-2023-9117. http://www.minsocam.org/

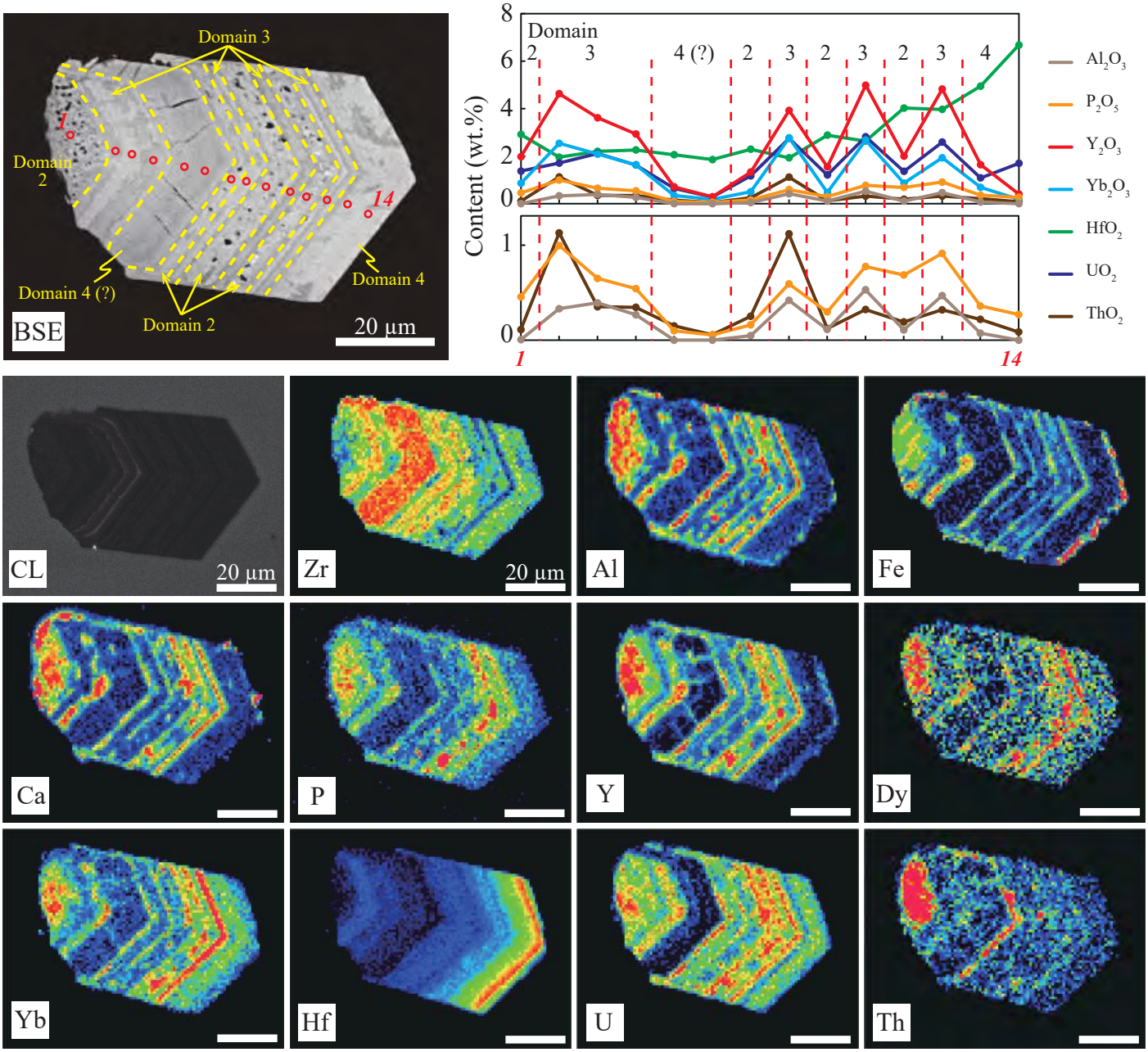

Figure 8

This is the peer-reviewed, final accepted version for American Mineralogist, published by the Mineralogical Society of America.
The published version is subject to change. Cite as Authors (Year) Title. American Mineralogist, in press.
DOI: https://doi.org/10.2138/am-2023-9117. http://www.minsocam.org/

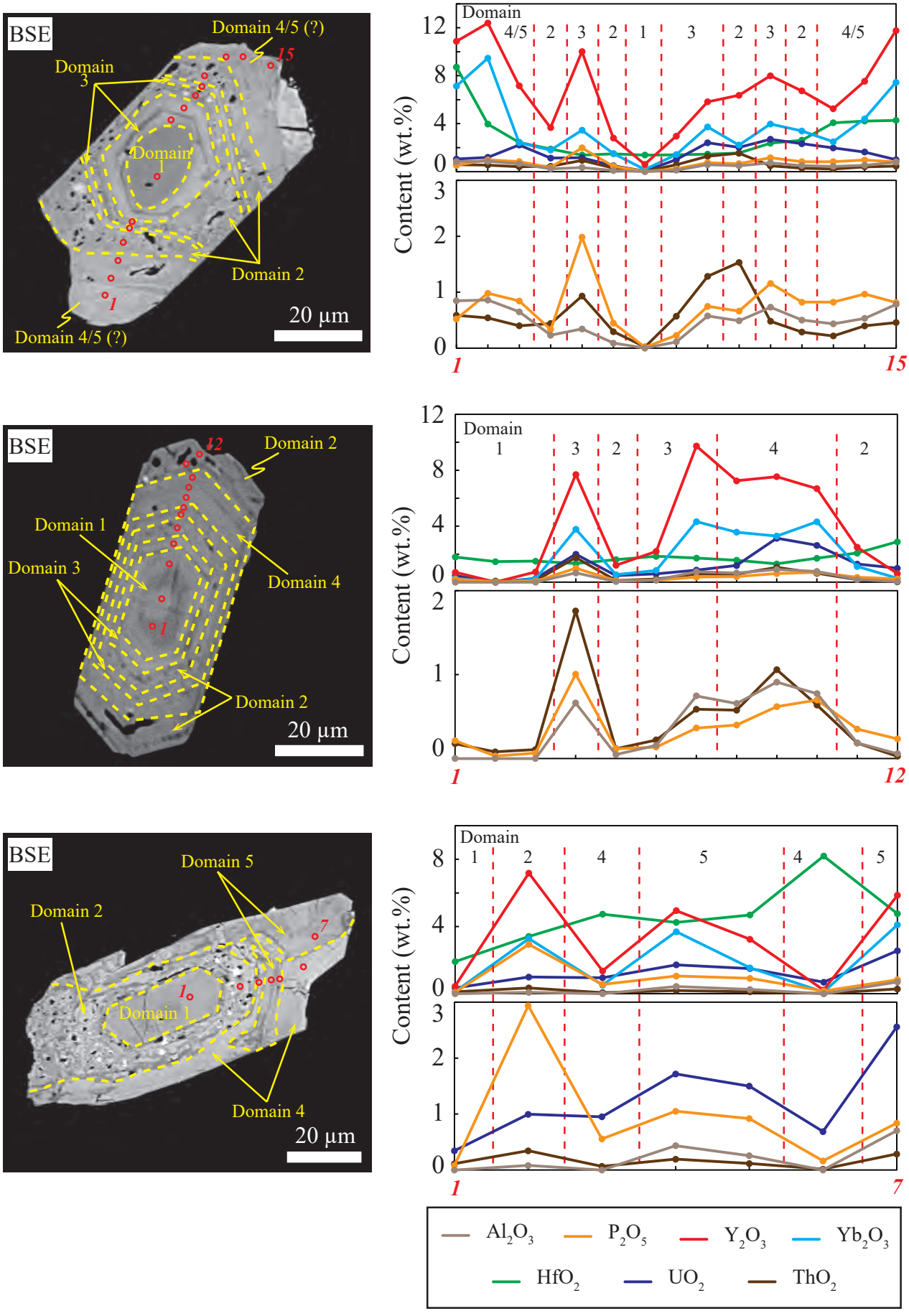

Figure 9

This is the peer-reviewed, final accepted version for American Mineralogist, published by the Mineralogical Society of America.
The published version is subject to change. Cite as Authors (Year) Title. American Mineralogist, in press.
DOI: https://doi.org/10.2138/am-2023-9117. http://www.minsocam.org/

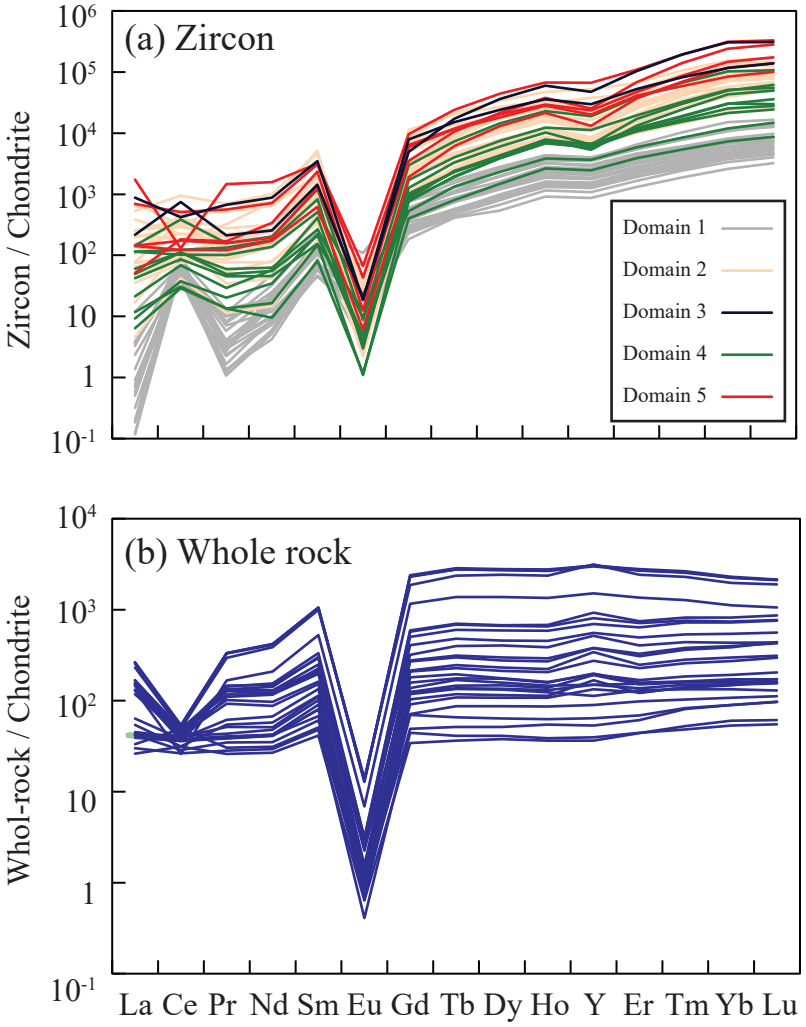

Figure 10

This is the peer-reviewed, final accepted version for American Mineralogist, published by the Mineralogical Society of America.
The published version is subject to change. Cite as Authors (Year) Title. American Mineralogist, in press.
DOI: https://doi.org/10.2138/am-2023-9117. http://www.minsocam.org/

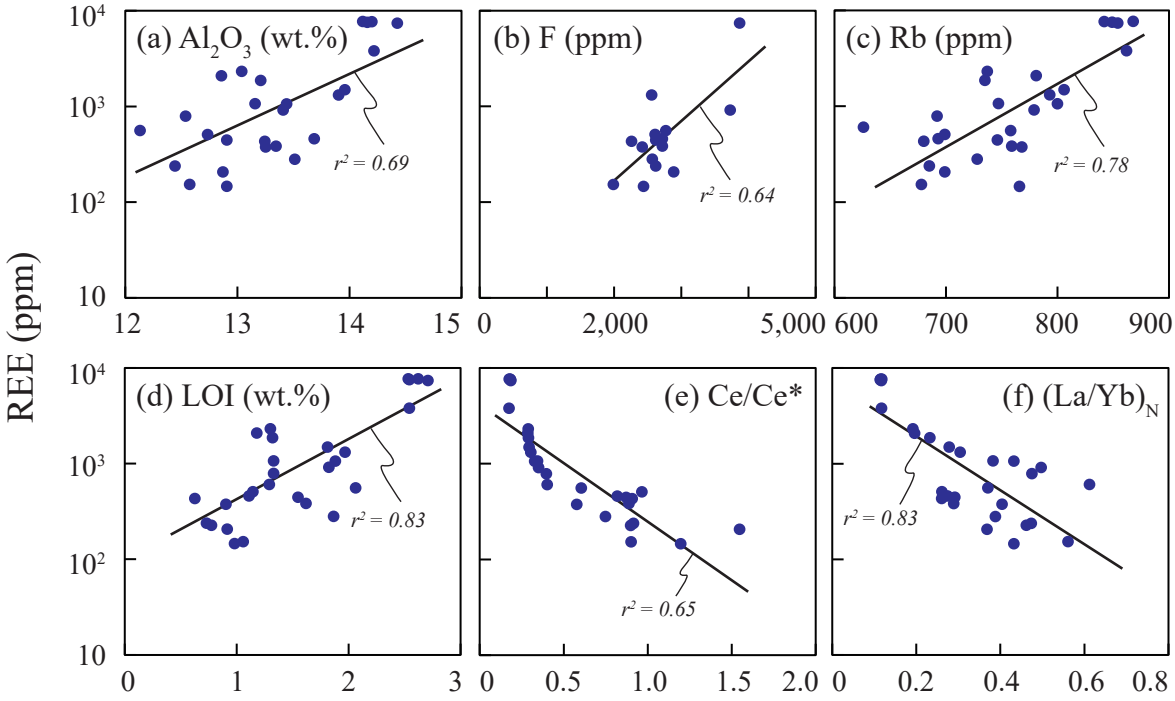

Figure 11

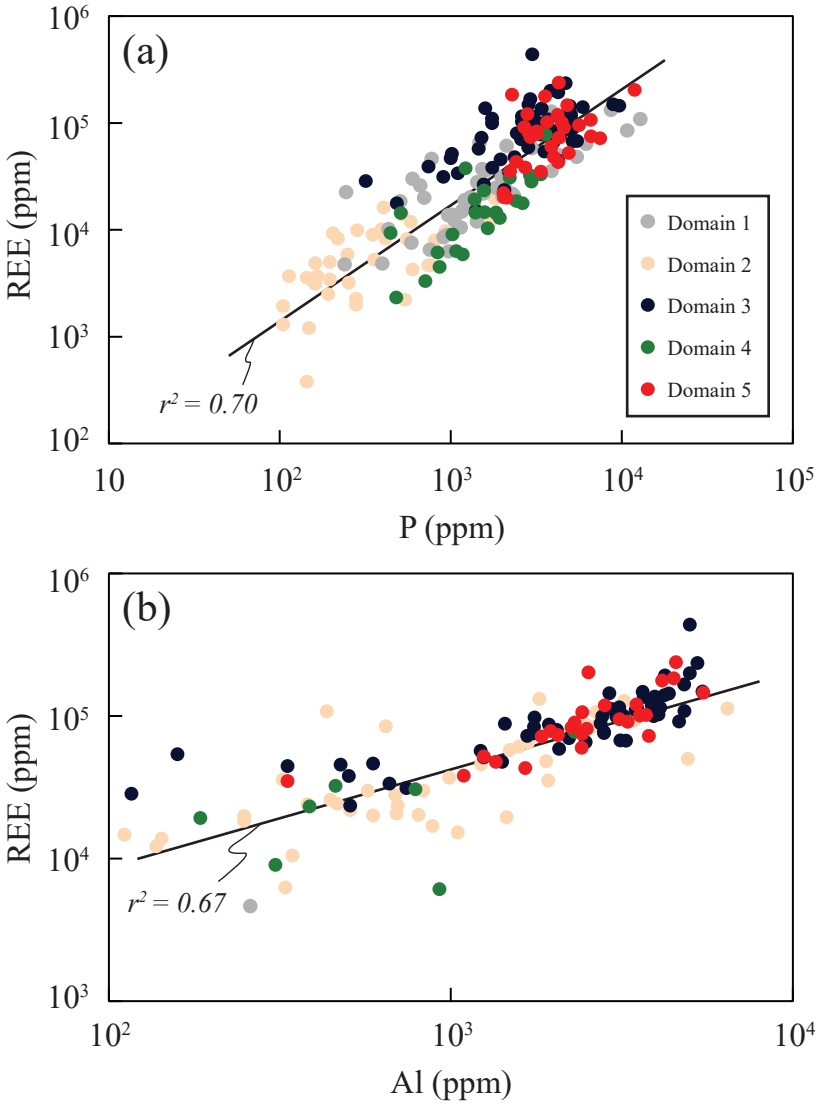

Figure 12

(a)

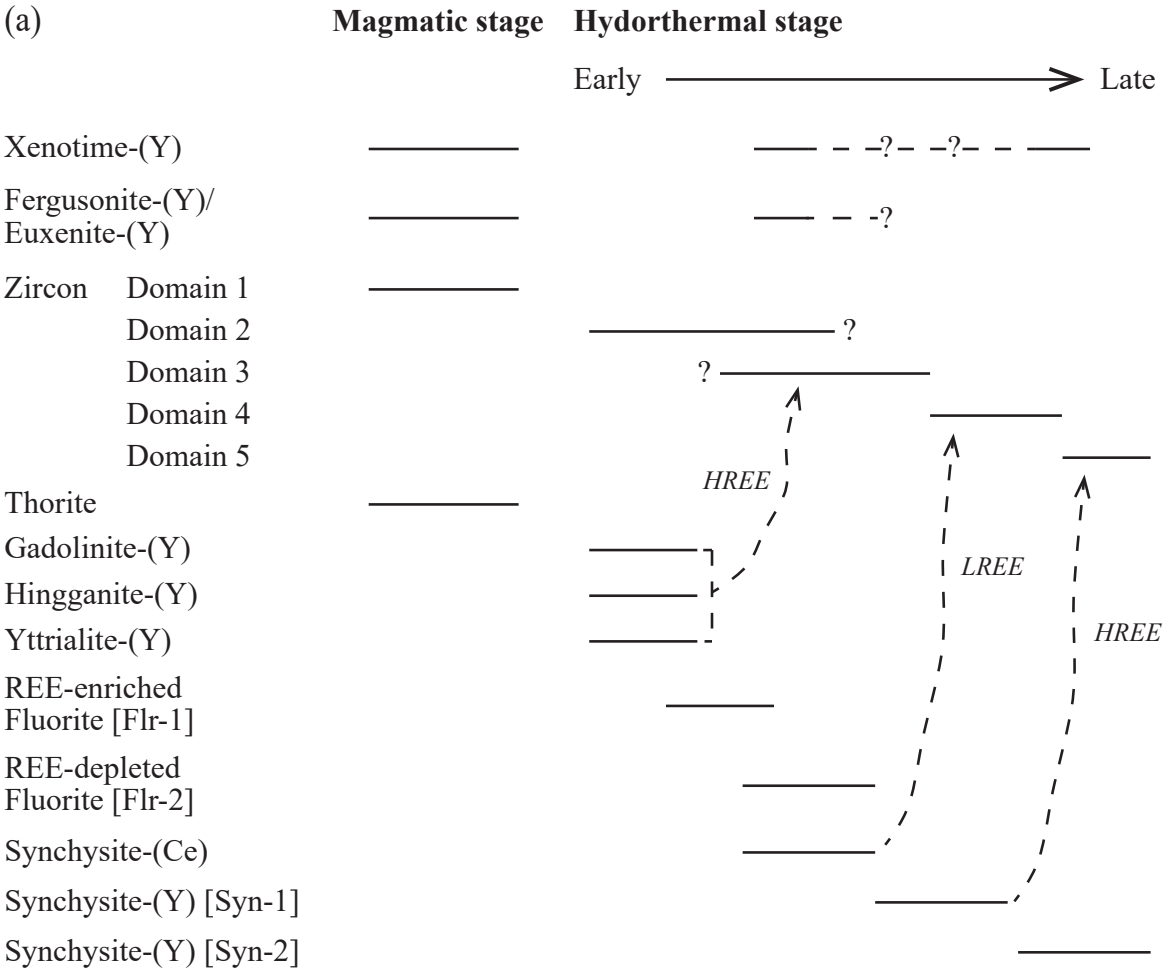

(b)

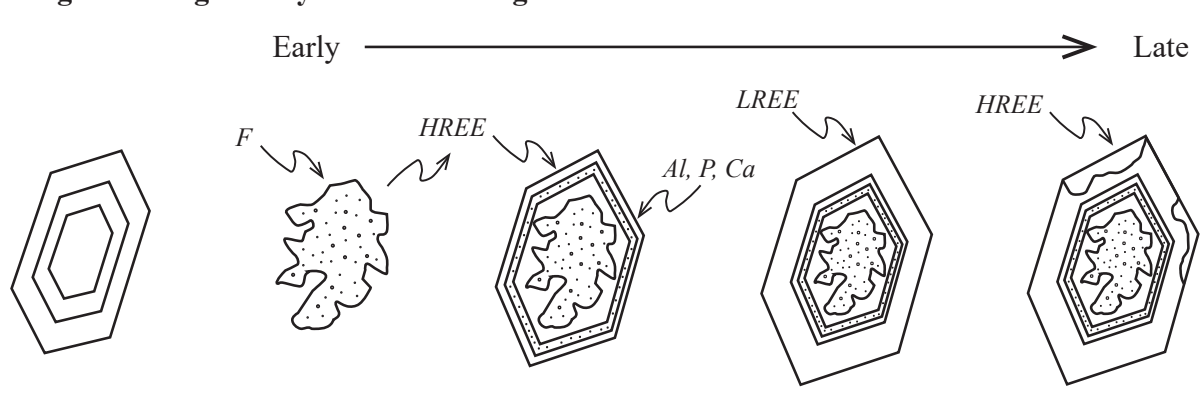

Domain 1
Magmatic growth with oscillatory zoning

Domain 2
CDP of magmatic Domain 1 by attack of F-rich fluid

Domain 2 & 3
Fluctuating F activity in fluid causing alternating CDP and continuous growth of zircon bands

Domain 4
Continuous growth of zircon in a relatively low F activity fluid

Domain 5
Diffusion-reaction process with fluid

Figure 13